# Second-Harmonic Generation as a Tool for Studying Electronic and Magnetic Structures of Crystals: Review

3 authors, including:

Manfred Fiebig
ETH Zurich
**297** PUBLICATIONS **21,381** CITATIONS

SEE PROFILE

R. V. Pisarev
Russian Academy of Sciences
**302** PUBLICATIONS **9,924** CITATIONS

SEE PROFILE

Some of the authors of this publication are also working on these related projects:

Low energy consuming spintronics using oxide thin films View project

Resonant optical magnetoelectric effect in magnetic nanostructures View project

# Second-harmonic generation as a tool for studying electronic and magnetic structures of crystals: review

**Manfred Fiebig**

*Max-Born-Institut, Max-Born-Straße 2A, 12489 Berlin, Germany*

**Victor V. Pavlov and Roman V. Pisarev**

*A. F. Ioffe Physical Technical Institute, 26 Politekhnicheskaya Street, 194021 St. Petersburg, Russia*

Second-harmonic generation (SHG) in magnetically ordered crystals is reviewed. The symmetry of such crystals is determined by the arrangement of both the charges and the spins, so their contributions to the crystallographic and the magnetic structures, respectively, must be distinguished. Magnetic SHG is introduced as a probe for magnetic structures and sublattice interactions. The specific degrees of optical experiments—including spectral, spatial, and temporal resolution—lead to the observation of novel physical effects that cannot be revealed by other techniques of probing magnetism. These include local or hidden phase transitions, interacting magnetized and polarized sublattices and domain walls, and magnetic interfaces. SHG in various centrosymmetric and noncentrosymmetric crystal classes of antiferromagnetic oxides such as $Cr_2O_3$, hexagonal $RMnO_3$ (R = Sc, Y, In, Ho-Lu), magnetic garnet films, $CuB_2O_4$, CoO, and NiO, is discussed. © 2005 Optical Society of America

*OCIS codes:* 190.4720, 160.3820, 190.4180.

## 1. INTRODUCTION

The invention of lasers has radically affected the field of science and technology. Their development led to the invention and rapid promotion of nonlinear optics.[1–9] With manifold applications, nonlinear optical phenomena play a vital role in modern optics. Compared with linear optics, nonlinear optical processes reveal novel information about the electronic structure of solids because, based on the involvement of more than a single light field, additional experimental degrees of freedom are accessible. In the vast field of nonlinear optics second-harmonic generation (SHG), as the lowest-order nonlinear process, plays a particular role. Since in the leading electric-dipole (ED) order SHG is allowed only in noncentrosymmetric materials, great experimental efforts have been invested in the search for new noncentrosymmetric materials with large optical nonlinearities. On the other hand, SHG is sensitive to surface and interface states of centrosymmetric media owing to the breaking of inversion symmetry at the boundary.

Similar to breaking of space-inversion symmetry, the breaking of time-inversion symmetry by long-range magnetic ordering or an applied magnetic field leads to new contributions to SHG. These contributions can be used to probe the magnetic structure. In the 1960s nonlinear optical phenomena related to magnetic fields were analyzed in theoretical studies by Pershan[10] and Adler.[11] It was shown that breaking of space inversion by magnetic order may result in ED contributions to SHG, and corresponding point symmetry groups were given.[12] In particular, antiferromagnetic SHG contributions were predicted for $Cr_2O_3$. Sadly, this work never received

appropriate attention. Subsequent theoretical work was devoted to the phenomenological approach to higher-order magneto-optical tensors describing, e.g., harmonic and sum- and difference-frequency generation.[13,14] ED-type magnetic SHG was phenomenologically analyzed for various magnetic systems.[15–17] The influence of an external or intrinsic magnetic field on the nonlinear optical polarization[18–22] as well as novel nonlinear magneto-optical Kerr effects related to SHG[23–26] were studied theoretically.

The first attempt at experimental investigation of SHG induced by magnetic ordering was probably carried out with the ferroelectric antiferromagnet $BiFeO_3$.[27,28] However, evidence for an antiferromagnetic contribution to SHG remained ambiguous.[29] Search for magnetic SHG in garnet films was reported in Ref. 30. A breakthrough occurred when magnetic SHG, the sign of which changed with the direction of magnetization, was unambiguously shown for ferromagnetic iron surfaces.[31,32] Subsequently, SHG in magnetically ordered substances became a subject of intensive research. Magnetic SHG, sometimes not quite adequately termed the nonlinear magneto-optical Kerr effect, was successfully employed for studying magnetic surfaces, multilayers, interfaces, and nanoparticles.[9,33–37] It was further shown that spatial resolution makes magnetic SHG a useful tool for microscopy.[37–42] Finally, magnetic SHG was applied as probe for the ultrafast temporal evolution of magnetically ordered systems after excitation with an intense ultrashort laser pulse.[43] Demagnetization phenomena on time scales far below that of spin-lattice relaxation were observed. However, great care has to be taken in a

proper distinction between the dynamics of the magnetic order parameter and the magneto-optical detection process.[44,45]

This review is devoted to SHG in several classes of magnetically ordered dielectrics. Antiferromagnetic chromium oxide $Cr_2O_3$ became the first crystal in which ED SHG due to noncentrosymmetric antiferromagnetic ordering was observed.[46] In contrast to metallic magnetic films, where SHG is usually studied at selected photon frequencies, the main emphasis of this review is placed on spectroscopy. We show that magnetic SHG provides access to electronic energy levels within the $d$–$d$ absorption bands or above the fundamental bandgap. It can be used to discriminate among magnetic space groups of magnetically ordered crystals, which are indistinguishable to diffraction methods. Magnetic SHG is especially powerful in the case of antiferromagnets, where linear magneto-optical methods such as the Faraday effect in transmission and the Kerr effect in reflection[47,48] fail because of the absence of a macroscopic magnetization. SHG reveals unusual hidden magnetic-field-induced phase transitions in hexagonal manganites and provides an unique opportunity to visualize antiferromagnetic spin-reversal (180°) domains. The general nature of our technique, which is based only on application of symmetry arguments, allows us to observe the interaction between ferroelectric and antiferromagnetic domain walls. Further, SHG provides access to the mechanisms and dynamics of nonlinear interaction of light with solids, thus opening new degrees of freedom for studies of magnetically ordered materials.

Section 2 of this review is devoted to the phenomenology of SHG and derivation of nonlinear polarizations and selection rules. In Section 3 the experimental setup for SHG transmission measurements on magnetic compounds will be introduced. Sections 4–7 are devoted to SHG in different symmetry classes of magnetically ordered materials and is followed by conclusions in Section 8.

## 2. PHENOMENOLOGY OF SECOND-HARMONIC GENERATION

Electromagnetic waves traveling through a medium induce an electric polarization $\mathbf{P}$, magnetization $\mathbf{M}$, or quadrupole polarization $\hat{Q}$ at any frequency which is a linear combination of the frequencies of the incident waves. The induced multipole moments can be expressed as expansion with respect to the electric and magnetic fields $\mathbf{E}(\omega)$ and $\mathbf{H}(\omega)$ of the incident light waves:

$$\mathbf{P} \propto \chi^{ee}{:}\mathbf{E} + \chi^{em}{:}\mathbf{H} + \chi^{eee}{:}\mathbf{EE} + \chi^{eem}{:}\mathbf{EH}$$
$$+ \chi^{emm}{:}\mathbf{HH} + \mathcal{O}[(\mathbf{E}, \mathbf{H})^3], \tag{1}$$

$$\mathbf{M} \propto \chi^{me}{:}\mathbf{E} + \chi^{mm}{:}\mathbf{H} + \chi^{mee}{:}\mathbf{EE} + \chi^{mem}{:}\mathbf{EH}$$
$$+ \chi^{mmm}{:}\mathbf{HH} + \mathcal{O}[(\mathbf{E}, \mathbf{H})^3], \tag{2}$$

$$\hat{Q} \propto \chi^{qe}{:}\mathbf{E} + \chi^{qm}{:}\mathbf{H} + \chi^{qee}{:}\mathbf{EE} + \chi^{qem}{:}\mathbf{EH}$$
$$+ \chi^{qmm}{:}\mathbf{HH} + \mathcal{O}[(\mathbf{E}, \mathbf{H})^3]. \tag{3}$$

The induced multipole moments compose the source term

$$\mathbf{S} = \mu_0 \frac{\partial^2 \mathbf{P}}{\partial t^2} + \mu_0 \left( \nabla \times \frac{\partial \mathbf{M}}{\partial t} \right) - \mu_0 \left( \nabla \frac{\partial^2 \hat{Q}}{\partial t^2} \right) \tag{4}$$

of a light wave. The ED term ($\propto \mathbf{P}$) is the leading contribution to $\mathbf{S}$. It exceeds the magnetic-dipole (MD) term ($\propto \mathbf{M}$) and the electric-quadrupole (EQ) term ($\propto \hat{Q}$) by a factor $\lambda/a$, where $\lambda$ and $a$ are the wavelength of the light and the lattice constant of the crystal, respectively. Linear contributions in relations (1–3) denote dielectric shift, magnetic permeability, and the linear magnetoelectric effect.[49] In the case of the second-order nonlinearity, the ED mechanism is only allowed in noncentrosymmetric media.[6] The corresponding susceptibility $\chi^{eee}$ leads to sum- and difference-frequency generation, SHG, and optical rectification (dc effect).

For magnetically ordered materials the relation between the electric field $\mathbf{E}(\omega)$ of the fundamental light and the induced nonlinear polarization $\mathbf{P}(2\omega)$ in the ED approximation is shown in Fig. 1 and is given by

$$\mathbf{P}(2\omega) = \epsilon_0 (\chi^{(i)} + \chi^{(c)}){:}\mathbf{E}(\omega)\mathbf{E}(\omega), \tag{5}$$

where the time-invariant ($i$-type[50]) tensor $\chi^{(i)}$ and the time-noninvariant ($c$-type[50]) tensor $\chi^{(c)}$ are responsible for crystallographic and linear spin-dependent contributions to the nonlinear polarization, respectively. The $c$-type contributions are allowed only below the magnetic ordering temperature where the time-reversal symmetry is broken. The tensor components of $\chi^{(i)}$ and $\chi^{(c)}$ are uniquely defined by the crystallographic and magnetic structure of the crystal. In the presence of absorption both tensors are complex, thus allowing interference of the form

$$I(2\omega) \propto (|\chi^{(i)}|^2 + |\chi^{(c)}|^2 \pm 2|\chi^{(i)}||\chi^{(c)}|\cos|\varphi|)E^4(\omega), \tag{6}$$

with $\varphi$ as phase between $i$- and $c$-type susceptibilities. When the spin direction is reversed, $\varphi$ changes by 180°, and the sign of the interference term $2|\chi^{(i)}||\chi^{(c)}|\cos\varphi$ is reversed so that the $\pm$ in Eq. (6) distinguishes opposite 180° domains. As is discussed in Ref. 51, the time noninvariance of $\chi^{(c)}$ refers to noninvariance under spin reversal rather than time reversal. Application of time reversal to the SHG process denotes optical parametric oscillation rather than harmonic generation, and the involvement of dissipation does not allow application of
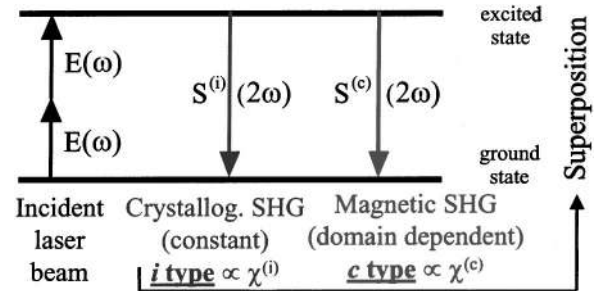


Fig. 1. Electric-dipole-type SHG in magnetically ordered crystals. A time invariant ($i$-type) source term, which is sensitive to the spinless crystallographic lattice, and a time noninvariant ($c$-type) source term, which is sensitive to the spin lattice, i.e. the magnetic structure, interfere, thus constituting the total SHG signal.

time reversal in the first place. Note that the interference of crystallographic and magnetic contributions to SHG conserves both amplitude and phase of the involved light fields, which will allow us to detect subtle nuances of magnetic structure such as the distribution of 180° domains.

The relation of SHG to ferroelectric or magnetic long-range order is expressed by the expansion

$$\chi^{(i)} = \chi(0) + \alpha{:}\mathbf{P}_S + \mathcal{O}[\mathbf{P}_S^2], \tag{7}$$

$$\chi^{(c)} = \beta{:}\mathbf{F}_M + \gamma{:}\mathbf{P}_S\mathbf{F}_M + \mathcal{O}[(\mathbf{P}_S, \mathbf{F}_M)^2]. \tag{8}$$

$\mathbf{P}_S$ is a polar vector describing pyroelectric polarization, and $\mathbf{F}_M$ is an axial vector in the case of ferromagnetic or ferrimagnetic crystals or a tensors of rank 1–3 in the case of antiferromagnetic crystals.[52]

The leading-order contribution to SHG, the ED transition, is allowed only in noncentrosymmetric media. A simple way to induce SHG in centrosymmetric media is an electric field, which because of its polar nature breaks inversion symmetry.[53] Such an electric-field-induced second harmonic (EFISH) was used to study, e.g. the space-charge region of semiconductor heterostructures or build quasi-phasematching devices.[54] In contrast, the axial nature of a magnetic field breaks time-inversion symmetry and should lead to new magnetic-field-induced second-harmonic (MFISH) contributions, allowing one to probe the spin (in contrast to the charge) of the electron. Similar to Eqs. (7) and (8), the coupling of SHG to static external electric fields $\mathbf{E}(0)$ or magnetic fields $\mathbf{H}(0)$ is written as

$$\chi^{(i)} = \eta{:}\mathbf{E}(0) + \nu{:}\mathbf{H}(0)\mathbf{F}_M + \mathcal{O}[(\mathbf{E}(0), \mathbf{H}(0))^2], \tag{9}$$

$$\chi^{(c)} = \sigma{:}\mathbf{H}(0) + \varsigma{:}\mathbf{E}(0)\mathbf{H}(0) + \tau{:}\mathbf{H}(0)\mathbf{P}_S$$
$$+ \upsilon{:}\mathbf{E}(0)\mathbf{F}_M + \mathcal{O}[(\mathbf{E}(0), \mathbf{H}(0))^2]. \tag{10}$$

The terms $\eta{:}\mathbf{E}(0)$ and $\sigma{:}\mathbf{H}(0)$ describe pure EFISH and MFISH contributions, respectively. The term $\eta{:}\mathbf{E}(0)$ was first observed in Ref. 55. The term $\sigma{:}\mathbf{H}(0)$ is discussed in this review for the case of $CuB_2O_4$. The cross terms $\nu{:}\mathbf{H}(0)\mathbf{F}_M$, $\varsigma{:}\mathbf{E}(0)\mathbf{H}(0)$, $\tau{:}\mathbf{H}(0)\mathbf{P}_S$, and $\upsilon{:}\mathbf{E}(0)\mathbf{F}_M$ in Eqs. (9) and (10) have not been observed yet.

Three types of MFISH can be distinguished[56]: (A) disordered materials or sublattices, where the applied magnetic field reduces symmetry in a perturbative way, thus inducing new contributions to SHG. The only known example is a weak surface induced MFISH signal at a fixed frequency for Si.[57,58] (B) Magnetically ordered materials, where the magnetic field induces phase transitions, which lead to new SHG components. Antiferromagnetic SHG in the spin-flop phase of $Cr_2O_3$ (see Subsection 4.A.7.) and hexagonal manganites may serve as examples. (C) Magnetically ordered materials, where the magnetic field increases an existing SHG signal by creating a single-domain state with maximum magnetization. New SHG contributions are not induced. Processes of this type are reviewed in Refs. 37 and 59 with emphasis on ferromagnetic systems, whereas antiferromagnetic systems are emphasized in the present review.

## A. Noncentrosymmetric Crystallographic Structure, No Magnetic Order
The most important crystals for nonlinear optical applications are piezoelectrics. They possess noncentrosymmetric crystallographic structure. Well-known examples are crystalline quartz $SiO_2$ (with point group 32), $\beta$-$BaB_2O_4$ ($3m$), $BaTiO_3$ ($4mm$), $LiNbO_3$ ($3m$) and $KH_2PO_4$ ($\bar{4}2m$), which are all used for optical harmonic and parametric generation. For pyroelectric crystallographic structures the nonlinear susceptibility is an odd function of the spontaneous polarization: $\chi^{(i)} \propto \mathbf{P}_S$.

## B. Centrosymmetric Crystallographic Structure, Noncentrosymmetric Magnetic Order
Inversion symmetry can be broken by noncentrosymmetric antiferromagnetic order even in the case of centrosymmetric crystallographic structure. The best example is $Cr_2O_3$.[60] Below the Néel temperature $T_N = 307.6$ K, $Cr_2O_3$ is noncentrosymmetric (magnetic point group $\bar{3}m$), and $c$-type ED SHG is allowed. The nonlinear polarization is proportional to the antiferromagnetic order parameter $\chi^{(c)} \propto \mathbf{F}_M$. SHG in $Cr_2O_3$ has been described phenomenologically in Refs. 12 and 16 and observed experimentally in Ref. 46. Above and below $T_N$ magnetic ED SHG is supplemented by crystallographic MD SHG, which is described by $\mathbf{M}(2\omega) \propto \chi^{mee}{:}\mathbf{E}(\omega)\mathbf{E}(\omega)$. The interference of magnetic and crystallographic SHG in $Cr_2O_3$ will be discussed in Subsection 4.A.

## C. Noncentrosymmetric Crystallographic Structure, Centrosymmetric Magnetic Order
The term $\beta{:}\mathbf{F}_M$ in Eq. (8) is responsible for magnetization-induced SHG in PtMnSb,[32] magnetic garnet films,[61] and $GaFeO_3$.[62] Although the bulk garnet structure is centrosymmetric (point group $m3m$), inversion symmetry is broken in thin epitaxial garnet films. This has been proved by observations of the linear magnetoelectric effect[63–65] and SHG in magnetic garnet films.[30,61,66–68]

The terms $\alpha{:}\mathbf{P}_S$ and $\gamma{:}\mathbf{P}_S\mathbf{F}_M$ have been studied in hexagonal $RMnO_3$ (R = Sc, Y, In, Ho, Er, Tm, Yb, Lu).[69–72] At room temperature the compounds possess the ferroelectric point group $6mm$, which allows ED SHG. At $T_N = 70$–123 K, triangular antiferromagnetic ordering of the $Mn^{3+}$ spins occurs, which leads to eight different magnetic symmetries as subgroups of $6mm$, three of which are centrosymmetric. For such structures there are two possible contributions to SHG. One contribution originates in the ferroelectric order, the nonlinear susceptibility being an odd function of the spontaneous polarization: $\chi^{(i)} \propto \mathbf{P}_S$. The second contribution appears only in the magnetically ordered phase and is a bilinear function of the spontaneous polarization and antiferromagnetic order parameter: $\chi^{(c)} \propto \mathbf{P}_S\mathbf{F}_M$.[52] This topic will be discussed in Subsection 5.A.

## D. Noncentrosymmetric Crystallographic Structure, Noncentrosymmetric Magnetic Order
In hexagonal manganites with R = Ho–Yb, antiferromagnetic $Mn^{3+}$ ordering is supplemented by ferromagnetic, ferrimagnetic, or antiferromagnetic rare-earth ordering at ~5 K.[73–78] Magnetic and magnetoelectric

sublattice interactions that may be supported by applied magnetic or electric fields lead to transitions into the magnetic phases $6mm$, $6\underline{mm}$, 6, $\underline{3}$, and 3. In these groups both the charge and the spin lattices are noncentrosymmetric, so that $i$-type and $c$-type ED SHG with linear coupling to, respectively, the ferroelectric or the magnetic order parameter is allowed aside from the aforementioned bilinear contribution. However, an ED contribution $\chi^{(c)} \propto \mathbf{F}_M$ has not been observed yet.

Another compound with noncentrosymmetric crystallographic structure and noncentrosymmetric magnetic order is $CuB_2O_4$, in which both magnetic and crystallographic ED SHG have been observed. The noncentrosymmetric structure is inherent to the crystal lattice and therefore parameterized by $\chi^{(i)}(0)$, while the antiferromagnetic order leads to a contribution $\chi^{(c)} \propto \mathbf{F}_M$, as is discussed in Subsection 6.A.

### E. Centrosymmetric Crystallographic Structure, Centrosymmetric Magnetic Order

SHG in centrosymmetric structures is forbidden in the ED approximation but allowed as MD or EQ process. Several theoretical[6,13,14,79–83] and experimental[84–88] studies take into account nonlocal nonlinear contributions to SHG. In spite of their higher-order nature, MD and EQ processes can be large enough to be detected in the region of electronic transitions. It was shown that magnetic ED SHG [$\propto \chi^{eee(c)}$] and crystallographic MD SHG [$\propto \chi^{mee(i)}$] can be of the same order of magnitude.[89–93] MD SHG in the centrosymmetric antiferromagnets CoO, NiO, and $KNiF_3$ was found to be very efficient because of multiple resonance enhancement of the different single-photon transitions making up the SHG process.[94–97] The nonlinear polarization in these compounds is given by $\mathbf{P}(2\omega) \propto \chi^{eem(i)}:\mathbf{E}(\omega)\mathbf{H}(\omega)$. Although the corresponding SHG signal is observed only below $T_N$ and is thus due to magnetic ordering, the SHG susceptibility is nonetheless time invariant because of quadratic coupling to the antiferromagnetic order parameter: $\chi^{(i)} \propto (\mathbf{F}_M)^2$. This will be the topic of Subsection 7.A.

## 3. EXPERIMENTAL DETAILS

For SHG experiments (see Fig. 2) a transmission setup with a two-stage $\beta$-$BaB_2O_4$ (BBO)-operated optical parametric oscillator (OPO) pumped by the third harmonic of a Nd:YAG laser was used as light source.[71] In the first stage emission from a BBO-operated seeder oscillator was spectrally narrowed by passing it through a monochromator. The light from the first stage was synchronized spatially, temporally, and spectrally with the BBO OPO in stage two in order to achieve seeded narrowband emission with a width of $\Delta E = 0.02$ meV from the power oscillator at the wavelength of the seeder oscillator. Samples were illuminated by 2–5-mJ, 3–8-ns light pulses with a photon energy of 0.6–1.6 eV and at a repetition rate of 10–40 Hz. A Glan–Taylor prism, wave plates, and optical long-pass filters were used to set the polarization of the incoming light and to block higher harmonics generated in the optical components. Short-pass and polarizing filters were used to separate the fundamental and the SHG light behind the sample and analyze the polarization of the SHG
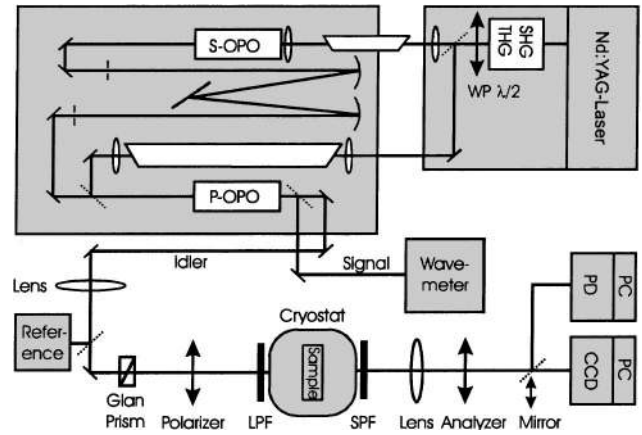


Fig. 2. Transmission setup for SHG spectroscopy and polarimetry. The laser source is a two-stage optical parametric oscillator pumped by the third harmonic of a pulsed Nd:YAG laser. THG, third harmonic generation at 3.495 eV (3 ns pulses at 10–40 Hz); S- or P-OPO, seeder or power OPO; WP, wave plate; LPF, SPF, long-, short-pass filter; PD, photodiode; CCD, camera; PC, computer.

signal. A telephoto lens was used to project the signal light onto a cooled CCD camera, where it was integrated in spectroscopic or spatially resolved in topographic experiments. In the case of 180° domains SHG from opposite domains differs only by a 180° phase shift of the nonlinear polarization, and both the amplitude and the phase of the signal wave have to be detected. This was achieved by an interferometric setup with achromatic beam imaging, which is described in Refs. 98 and 99.

## 4. SHG IN CENTROSYMMETRIC CRYSTALLOGRAPHIC STRUCTURES WITH NONCENTROSYMMETRIC MAGNETIC ORDER

### A. Magnetoelectric Antiferromagnet $Cr_2O_3$

*1. Crystallographic and Magnetic Structure of $Cr_2O_3$*
$Cr_2O_3$ crystallizes in the centrosymmetric point group $\bar{3}m$ with two formula units per unit cell[100] (see Fig. 3). The four chromium ions are at 4c sites of symmetry 3. Below $T_N = 307.6$ K, the magnetic point group is $\underline{\bar{3}m}$. In zero magnetic field the four $Cr^{3+}$ spins are aligned along the rhombohedral optical axis in an alternating sequence of up and down spins.[101] Although space- and time-reversal symmetry are broken by this antiferromagnetic arrangement, the combined space–time reversal remains a symmetry element. Figure 3(b) shows the two 180° domains.

*2. Electronic Structure and Linear Optical Properties*
The electronic energy level diagram is shown in Fig. 4(a). The ground state is $^4A_2(t_2^3)$, in which each of the three $d$ electrons occupies three different $t_2$ orbitals with parallel spins. The energy-level structure of $Cr^{3+}$ is derived from $Al_2O_3{:}Cr^{3+}$ (ruby) as a dilute paramagnetic isomorph of $Cr_2O_3$.[102,103] Optical absorption in $Cr_2O_3$ is characterized by two intense broad bands, which are caused by spin-allowed $^4A_2(t_2^3) \rightarrow {}^4T_2(t_2^2e)$ and $^4A_2(t_2^3) \rightarrow {}^4T_1(t_2^2e)$ transitions. Their oscillator strength is of

the order of $10^{-2}$, which is approximately 2 orders of magnitude higher than in the case of ruby. Breaking inversion symmetry makes the electric dipole transitions between the $3d$ levels allowed. Therefore the octahedral cubic terms are actually a set of levels located in the energy range $\Delta E < v \simeq 0.1$ eV, where $v$ is the characteristic energy of the trigonal field. The broad bands are supplemented by several sharp lines associated with spin-forbidden $^4A_2(t_2^3) \to {}^2E(t_2^3)$, $^4A_2(t_2^3) \to {}^2T_1(t_2^3)$, and $^4A_2(t_2^3) \to {}^2T_2(t_2^3)$ transitions. The lines represent Frenkel excitons, Davydov splitting, and exciton-magnon transitions.[103–107] Although being less intense than the spin-allowed transitions, they are characterized by relatively strong absorption coefficients $\alpha \sim 10^3$ cm$^{-1}$.[107] Charge transfer as measured by two-photon absorption begins above 3.44 eV.[108]

### 3. Phenomenology of SHG

With $\bar{3}m$ as magnetic symmetry, axial $i$ tensors and polar $c$ tensors of odd rank are allowed in $Cr_2O_3$.[50] This leads to two independent components each for MD SHG and ED SHG which are given by $\chi^{m(i)} \equiv \chi^{mee(i)}_{yyy} = -\chi^{mee(i)}_{yxx} = -\chi^{mee(i)}_{xyx} - \chi^{mee(i)}_{xxy}$, $\chi^{mee(i)}_{xyz} = \chi^{mee(i)}_{xzy} = -\chi^{mee(i)}_{yxz} = -\chi^{mee(i)}_{yzx}$ and $\chi^{e(c)} \equiv \chi^{eee(c)}_{yyy} = -\chi^{eee(c)}_{yxx} = -\chi^{eee(c)}_{xyx} - \chi^{eee(c)}_{xxy}$, $\chi^{eee(c)}_{xyz} = \chi^{eee(c)}_{xzy} = -\chi^{eee(c)}_{yxz} = -\chi^{eee(c)}_{yzx}$, respectively.[50] For light propagating along the optical $z$ axis the induced source term in a circular basis is given by[46]

$$\mathbf{S}(2\omega) = \begin{pmatrix} S_+ \\ S_- \\ S_z \end{pmatrix} = 4\sqrt{2}\frac{\omega^2}{c^2} \begin{pmatrix} [-\chi^{m(i)} + i\chi^{e(c)}]E_-^2 \\ [\chi^{m(i)} + i\chi^{e(c)}]E_+^2 \\ 0 \end{pmatrix}. \quad (11)$$

For circularly polarized fundamental light at intensity $I(\omega) \propto |E_\pm|^2$ the SHG intensity $I(2\omega) \propto |\mathbf{S}|^2$ as function of circular polarization ($\sigma = \pm 1$) and direction of the antiferromagnetic vector ($l = \pm 1$)[109] is given by

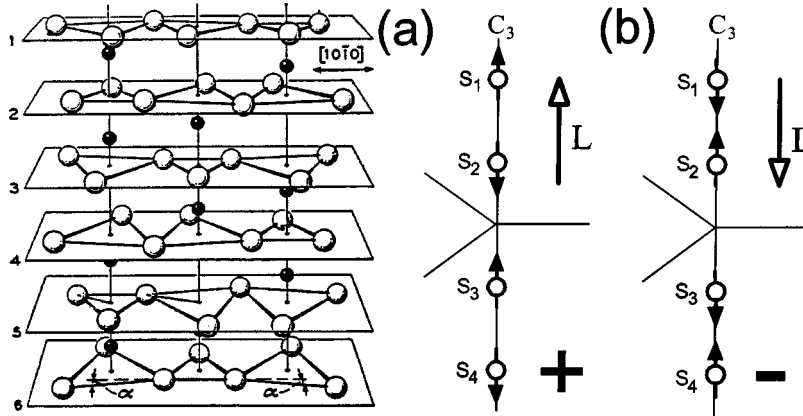$$I(2\omega) \propto I(\omega)^2[|\chi^{m(i)}|^2 + |\chi^{e(c)}|^2 - l\sigma \cdot \Delta], \quad (12)$$



Fig. 3. (a) Crystallographic and (b) magnetic structure of $Cr_2O_3$. (a) $Cr^{3+}$ ions (black) are surrounded by six $O^{2-}$ ligands (white) in a distorted octahedral with site symmetry 3. (b) Two antiferromagnetic 180° domains with a $+ - + -$ or $- + - +$ sequence of spins along the trigonal axis are formed, thus defining the antiferromagnetic vector $\mathbf{l}$.
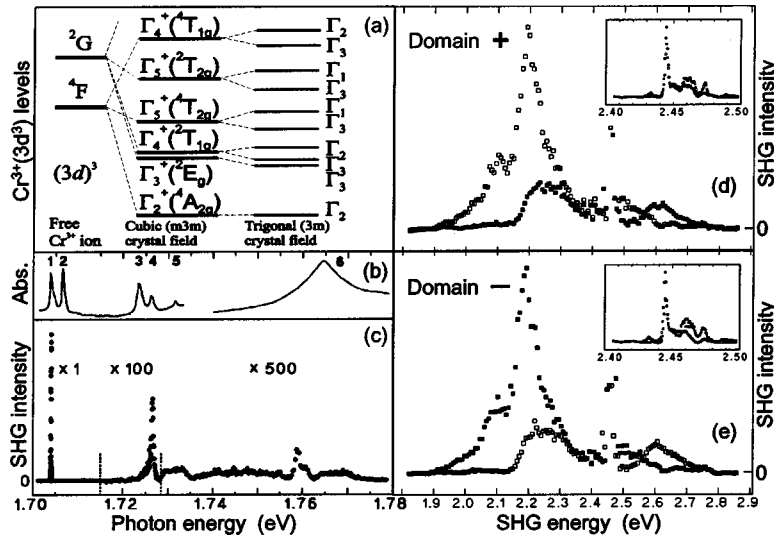


Fig. 4. Energy levels, linear absorption, and SHG spectra of $Cr_2O_3$. (a) Energy levels of $Cr^{3+}(3d^3)$ electrons in the trigonally distorted octahedral ligand field of $Cr_2O_3$. (b) Linear absorption spectrum of $Cr_2O_3$ at 77 K; lines 1–5 from Ref. 106, line 6 from Ref. 105. (c) SHG spectrum at 10 K for light incident along the trigonal $z$ axis. (d), (e) SHG spectra of $Cr_2O_3$ on different locations on the sample. Filled and open squares refer to, respectively, right and left circularly polarized light which is incident along $z$.

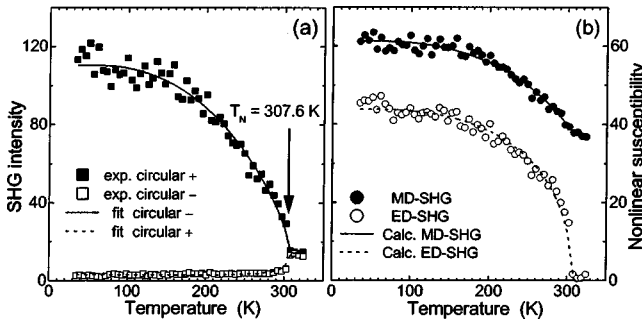Fig. 5.  Temperature dependence of SHG for light incident along *z*.  (a) Interference between *c*-type ED SHG and *i*-type MD SHG with circularly polarized light for SHG at 2.1 eV.  (b) Corresponding contributions from *c*-type ED SHG and *i*-type MD SHG. The curves are fits of $\chi^{e(c)} \propto l(T)$ and $\chi^{m(i)} \propto b + cl(T)^2$ to the temperature dependence (see text).

where $\Delta = \mathrm{sgn}(l)[\chi^{m(i)\prime}\chi^{e(c)\prime\prime} - \chi^{m(i)\prime\prime}\chi^{e(c)\prime}]$.  The sign of the interference contribution $l\sigma \cdot \Delta$ can be changed either by reversing the circular polarization $\sigma$ or the antiferromagnetic vector **l**.

## 4.  Spectroscopy
Figure 4(c) shows the SHG spectra at 8 K in the region of the $^4A_2 \rightarrow {}^2E$, $^2T_1$ transitions.  Whereas in the linear absorption spectra[103,104,106,107] the intensities of lines 1–5 are of the same order of magnitude, line 1 at 1.704 eV reveals a SHG intensity that is 2–3 orders of magnitude higher than for the other lines.  The 1.704-eV line is $\sigma$ polarized and has a spectral width of only 40 $\mu$eV.  Weaker SHG lines correspond to $\sigma$-polarized lines 4 and 5.  No SHG was detected for $\pi$-polarized lines 2 and 3.  Lines 1, 4, and 5 obey the selection rules of an ED transition. There was no dependence of SHG intensity on the circular polarization of the incoming light, which means that only the $|\chi^{e(c)}|^2$ contribution to SHG is effective in this part of the spectrum.

Figures 4(d) and 4(e) show the polarization-dependent SHG spectra at $T = 10$ K in the range 1.8–2.9 eV.  According to Fig. 4(a) this range includes the spin-allowed $^4A_2 \rightarrow {}^4T_2$ and $^4A_2 \rightarrow {}^4T_1$ transitions as well as the spin-forbidden $^4A_2 \rightarrow {}^2T_2$ transition.  As expected from Eq. (11), the SHG light is circularly polarized but with opposite helicity with respect to the incoming light.  In contrast to the SHG spectra of the $^4A_2 \rightarrow {}^2E$, $^2T_1$ transitions, a pronounced polarization dependence is observed. Figure 5(a) shows that the total SHG intensity decreases with temperature until a stable nonzero value is reached at $T_N = 307.6 \pm 0.1$ K and also shows the disappearance of the circular polarization dependence.  Above $T_N$, SHG in the region of the $^4A_2 \rightarrow {}^4T_2$ transitions obeys the selection rules of MD SHG.

The rather spectacular behavior is fully explained by relation (12).  Above $T_N$ only $|\chi^{m(i)}|^2$ contributes to the SHG signal.  Because $\Delta = 0$, no polarization dependence is expected.  Below $T_N$ $\chi^{e(c)}$ also contributes to SHG. The pronounced polarization dependence points to an interference between magnetic ED and crystallographic MD SHG contributions of approximately equal amplitude.  To model the temperature dependence of the interference contribution, we assume that the ED contribution depends linearly on the order parameter, $\chi^{e(c)} \propto l(T)$,

whereas the MD contribution consists of a constant term and a term with quadratic coupling to the order parameter:  $\chi^{m(i)} \propto b + cl(T)^2$.  The quadratic term is due to secondary effects such as magnetostriction.  From the temperature variations of the order parameter in $Cr_2O_3$,[110] the temperature dependence of the electric and magnetic dipole contributions was calculated as shown in Fig. 5(b).

## 5.  Discussion and Microscopical Models
Microscopic models for $\chi^{e(c)}$ and $\chi^{m(i)}$ that explain the interference and approximately equal amplitude of magnetic ED and crystallographic MD contributions to SHG were developed by two groups.[90–93]  In both theories calculations are based on the orbital $d$ wave functions of free $Cr^{3+}$ ion, which are perturbed and mixed by the trigonal distortion of the octahedral ligand field exerted on the $Cr^{3+}$ ion by the next $O^{2-}$ neighbors, which can be described by the twisting term $y(3x^2 - y^2)$.[93]  Spin–orbit interaction mediates the coupling between the $Cr^{3+}$ spins and the light waves at $\omega$ and $2\omega$.  One of the theories[92,93] goes further and takes excitonic exchange between neighboring $Cr^{3+}$ ions into account.

## 6.  Antiferromagnetic Domain Structure
Since the sign of the antiferromagnetic order parameter corresponds to the sign of the interference term in relation (12), opposite 180° domains are recognized by their different brightness.  Figure 6 shows a $Cr_2O_3$ sample at 295 K imaged with SHG light at 2.16 eV.  Two regions with different brightness corresponding to the opposite domains are visible.  Domains have a lateral size of $\sim$100 $\mu$m.  A discontinuous change of brightness occurs at the domain boundaries, which do not follow any of the principal crystallographic directions.  As expected the domain structure vanishes at $T_N$.  Reversing the sample showed that on the opposite surface the same distribution of domains is observed, which confirms that domains extend along the $z$ axis all through the sample.

## 7.  Magnetic Field Dependence
In a magnetic field $B_{SF} = 5.8$ T, spins in $Cr_2O_3$ flop from the trigonal $z$ axis into the $xy$ plane, in which they may be oriented along the $x$, the $y$, or some in-between $\rho$ direction, each case corresponding to a different magnetic symmetry.  Since there are three sets of $x$ and $y$ axes for the
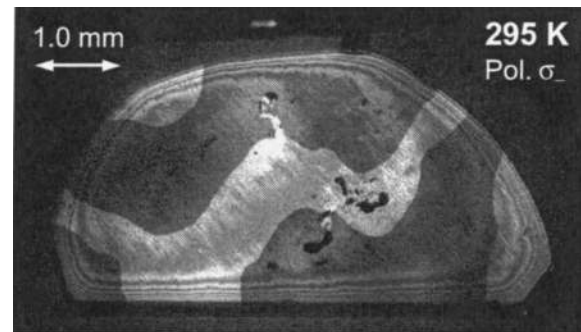


Fig. 6.  Antiferromagnetic 180° domains in $Cr_2O_3$ exposed to circularly polarized light for SHG at 2.1 eV.  Exposure time was 35 min but was reduced to 1–5 min in subsequent experiments.
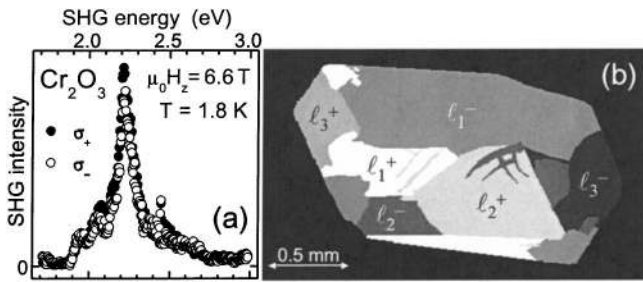
Fig. 7.   (a) SHG spectrum of $Cr_2O_3$ in the spin-flop phase taken with circularly polarized light incident along the $z$ axis.   (b) Distribution of the six orientational domains, $\ell_{1,2,3}^{\pm}$, that exist in the spin-flop phase.

trigonal crystal, six possible orientational domains can be realized.   The analysis of selection rules shows that with magnetic SHG (MSHG) all 18 resulting magnetic structures can be distinguished.[111]   Figure 7(a) shows the SHG spectrum of $Cr_2O_3$ at $B > B_{SF}$.   The circular polarization dependence that is characteristic for $Cr_2O_3$ in zero field is absent which, according to the MSHG selection rules, can be expected only if the $Cr^{3+}$ spins are aligned along the $y$ axes of the crystal, corresponding to the point symmetry $\underline{2}/m$.[111]   Images of the sample in the spin-flop state and further polarization analysis reveal all six orientational domains for the $S\|y$ case as shown schematically in Fig. 7(b).   In preceding publications, that were based on the determination of magnetic symmetry from the components of the magnetoelectric tensor,[112–115] domains were always neglected, which led to contradictory results.   Spatial resolution thus proves to be indispensable for a correct symmetry analysis.

## 5.   SHG IN NONCENTROSYMMETRIC CRYSTALLOGRAPHIC STRUCTURES WITH CENTROSYMMETRIC MAGNETIC ORDER

### A.   Ferroelectric Antiferromagnets

**$RMnO_3$ (R = Sc, Y, In, Ho, Er, Tm, Yb, Lu)**
Transition metal oxides, and among them the rare-earth manganites $RMnO_3$, form a very broad class of materials exhibiting a wide range of exotic structural, magnetic, electronic, and optical properties.   Attention has been focused on the doped orthorhombic perovskite manga-

nites,[116] which exhibit negative and unusually large magnetoresistance.   In terms of their chemical composition, undoped hexagonal and orthorhombic manganites are identical.   However, differences in crystal structures and in the symmetry of the local environment of the manganese and rare-earth ions lead to radically different physical properties.

### 1.   Crystallographic and Magnetic Structure
The crystal structure of the hexagonal manganites was first studied in Ref. 117 and then refined in a number of subsequent publications.[118–120]   The hexagonal unit cell is shown in Fig. 8.   The $R^{3+}$ ions occupy 2a positions (local symmetry $3m$) and 4b positions (local symmetry 3).   All the magnetic $Mn^{3+}(3d^4)$ ions occupy 6c positions (local symmetry $m$), which are characterized by an unusual distorted bipyramidal coordination to the nearest $O^{2-}$ neighbors.   The space group $P6_3cm$ is noncentrosymmetric and pyroelectric, and all compounds are ferroelectric with $T_C \approx 500$–$1000$ K.[121–124]   Ferroelectric ordering occurs in two steps at different temperatures with, respectively, tilting and distortion of the $MnO_5$ bipyramids.[124]   Ferroelectricity is neither of the $BaTiO_3$ type nor of the lone-pair type but geometrically driven, which explains the otherwise unfavorable coexistence of ferroelectricity and magnetic ordering.[125]

The magnetic properties arise primarily from the manganese ions $Mn^{3+}(3d^4)$ in the high-spin state with $S = 2$.   The possible magnetic structures of the $Mn^{3+}$ lattice and the magnetic phase transitions connecting them are shown in Fig. 9.   The magnetic order is dominated by antiferromagnetic in-plane Mn–O–Mn superexchange and is supplemented by a 2-order-of-magnitude weaker interplane Mn–O–O–Mn exchange in the stacked triangular lattice.[126,127]   Below $T_N = 73$–$124$ K, the strong superexchange leads to a $120°$ arrangement of $Mn^{3+}$ spins in the basal plane, which breaks the triangular frustration.   This leaves the spin angle $\varphi_{spin}$ between the $Mn^{3+}$ magnetic moment and the local $x$ axis as degree of freedom in the manifestation of the magnetic structure.   With $|\varphi_{spin}|$ equal to $0°$ or $90°$ and two opposite relative orientations of $Mn^{3+}$ spins in adjacent planes at $z = 0$ and $z = c/2$ along $z$, the four principal magnetic structures denoted $A_1$, $A_2$, $B_1$, $B_2$ are derived.   The symbols refer to the one-dimensional representations of the crys-
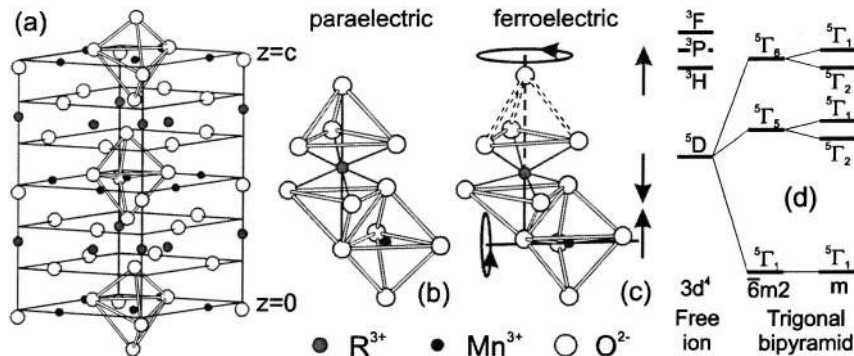


Fig. 8.   (a) Stereographic view of the ferroelectric $RMnO_3$ lattice.   (b), (c) Relation of the $R^{3+}$ and $Mn^{3+}$ cations and the position of the oxygen ligands for the paraelectric and ferroelectric case.   Arrows denote the movement of ions in the course of the two-stage[124] ferroelectric ordering; dashed lines indicate weakened interaction.   (d) Electronic levels of the fivefold coordinated $Mn^{3+}(3d^4)$ ion.
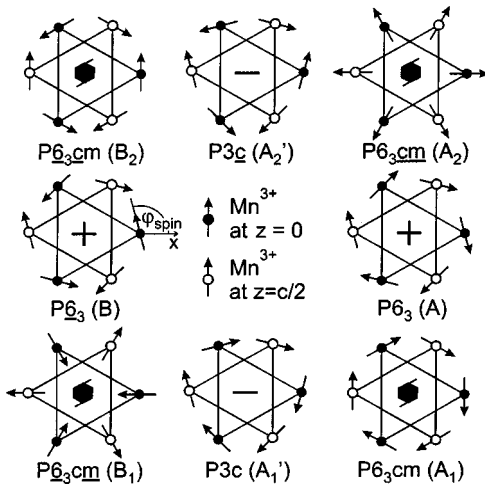
Fig. 9. Magnetic structures of hexagonal RMnO$_3$. Two types of triangular antiferromagnetic ordering with opposite orientation of Mn$^{3+}$ spins in adjacent planes along $z$ for A, A$_1'$ and B, A$_2'$ representations and two types of spin rotation with an equal ($+$, in phase) or opposite ($-$, antiphase) sense of rotation in adjacent planes along $z$ lead to a total of eight different magnetic structures. For each structure the magnetic point group and the one-dimensional representation describing the transformation properties of the Mn$^{3+}$ spins are given. Neighboring structures at the corners differ by $\pm 90°$ in $\varphi_{\rm spin}$. They are interconnected by an in-phase or antiphase spin rotation, which leads to the intermediate structures depicted for an (arbitrary) rotation of spins by $\pm 15°$ or $\pm 75°$.

tallographic space group, which describe the transformation properties of the spins.[128] Phase transitions between the principal structures can occur through an in-phase or an antiphase rotation of the Mn$^{3+}$ spins, for which the sense of rotation is, respectively, equal or opposite in adjacent basal Mn$^{3+}$ planes. The rotation leads to the intermediate magnetic structures denoted A, B, A$_1'$, A$_2'$. The rare-earth ions Ho$^{3+}$($4f^{10}$), Er$^{3+}$($4f^{11}$), Tm$^{3+}$($4f^{12}$), and Yb$^{3+}$($4f^{13}$) also contribute to the magnetic properties. Below $T_C = 5$–6 K, long-range ordering of the two rare-earth sublattices occurs,[73–78] which may be ferromagnetic, ferrimagnetic, or antiferromagnetic.[129]

## 2. Electronic Structure and Linear Optical Properties

The first experimental studies[69,130] revealed strong optical absorption in YMnO$_3$ above 1.28 eV at 295 K and above 1.55 eV at 4 K supplemented by transitions within the Ho$^{3+}$, Er$^{3+}$, Tm$^{3+}$, and Yb$^{3+}$ multiplets.[131] Thin-film absorption spectra of YMnO$_3$[132] suggested 4.2–4.3 eV as the fundamental absorption edge. Other linear and third-order spectroscopy data were reported.[133–137] The electronic transitions start at ∼1.1 eV, and the lowest excitation with an optical conductivity $\sigma$ of $\simeq 1100$–1500 $\Omega^{-1}$ cm$^{-1}$ is centered at ∼1.6 eV. Another strong broad band is observed near 5 eV. The band at 1.6 eV was contradictorily assigned to a symmetry-allowed on-site Mn $d$–$d$ transition[135] or to charge transfer from oxygen to manganese.[136] The electronic structure of the hexagonal manganites became a subject of theoretical studies only very recently.[125,138,139] The $^5D$ state of the Mn$^{3+}$ ion splits into a $^5\Gamma_1$ ground state and the excited $^5\Gamma_5$ and $^5\Gamma_6$ states under the influence of a crystal field with trigonal

bipyramidal symmetry $\bar{6}m2$. Local distortions lead to further reduction of symmetry as shown in Fig. 8(d). SHG opens a new possibility to probe hidden localized $d$–$d$ transitions that overlap with much stronger charge-transfer or interband transitions beginning above 1.4 eV, because at the frequency of the fundamental beam crystals are transparent, while only the SHG frequency falls into the spectral region of high absorption.

## 3. Phenomenology of SHG

According to previous work[126,127,140,141] only B-type magnetic structures from Fig. 9 are expected for RMnO$_3$ in the absence of applied fields. For the magnetic space group $P6_3\underline{c}m$, Table 1 leads to the time-invariant contribution $\mathbf{P}(2\omega) \propto \mathbf{P}_S$ with

$$\mathbf{P}^{(i)}(2\omega) = \epsilon_0 \begin{pmatrix} 2\chi_{xxz}^{(i)} E_x(\omega) E_z(\omega) \\ 2\chi_{xxz}^{(i)} E_y(\omega) E_z(\omega) \\ \chi_{zxx}^{(i)}[E_x^2(\omega) + E_y^2(\omega)] + \chi_{zzz}^{(i)} E_z^2(\omega) \end{pmatrix},$$

(13)

and to the time-noninvariant contribution $\mathbf{P}(2\omega) \propto (\mathbf{P}_S \cdot \mathbf{l})$ with

$$\mathbf{P}^{(c)}(2\omega) = \epsilon_0 \begin{pmatrix} \chi_{xxx}^{(c)}[E_x^2(\omega) - E_y^2(\omega)] \\ 2\chi_{xxx}^{(c)} E_x(\omega) E_y(\omega) \\ 0 \end{pmatrix}, \quad (14)$$

with $\mathbf{P}_S$ as the ferroelectric and $\mathbf{l}$ as the antiferromagnetic order parameters. Observation of crystalline SHG is possible only with participation of $z$-polarized fundamental or SHG light. In contrast, observation of magnetic SHG spectra depends on the presence of only $x$- or $y$-polarized fundamental and SHG light, for which light propagating along the $z$ axis is the most favorable configuration.

## 4. Spectroscopy

Figure 10 shows the crystallographic spectra of $\chi_{xxz}^{(i)}$, $\chi_{zzz}^{(i)}$, and $\chi_{zxx}^{(i)}$ in the 1.2–3.0-eV range of YMnO$_3$ at $T = 6$ K. The strongest SHG signal stems from the $\chi_{zxx}^{(i)}$ component, for which the position of the observed transitions are shifted by ∼0.2 eV toward higher energies in

## Table 1. Nonzero Tensor Components $\chi_{ijk}^{(2)}$ for ED-SHG in Hexagonal RMnO$_3$

| Space Group | Tensor Components |
|---|---|
| Crystalline SHG ($i$ type) | |
| $P6_3cm$ | $\chi_{xxz}^{(i)} = \chi_{xzx}^{(i)} = \chi_{yyz}^{(i)} = \chi_{yzy}^{(i)}$, $\chi_{zxx}^{(i)} = \chi_{zyy}^{(i)}$, $\chi_{zzz}^{(i)}$ |
| Magnetic SHG ($c$ type) | |
| $P6_3\underline{cm}$ | $\chi_{yyy}^{(c)} = -\chi_{yxx}^{(c)} = -\chi_{yyx}^{(c)} = -\chi_{xxy}^{(c)}$ |
| $P6_3\underline{c}m$ | $\chi_{xxx}^{(c)} = -\chi_{xyy}^{(c)} = -\chi_{yxy}^{(c)} = -\chi_{yyx}^{(c)}$ |
| $P6_3$ | $P6_3\underline{cm} \oplus P6_3\underline{c}m$ |
| $P6_3c\underline{m}$ | $\chi_{xyz}^{(c)} = \chi_{xzy}^{(c)} = -\chi_{yxz}^{(c)} = -\chi_{yzx}^{(c)}$ |
| $P6_3cm$ | $\chi_{xxz}^{(c)} = \chi_{xzx}^{(c)} = \chi_{yyz}^{(c)} = \chi_{yzy}^{(c)}$, $\chi_{zxx}^{(c)} = \chi_{zyy}^{(c)}$, $\chi_{zzz}^{(c)}$ |
| $P6_3$ | $P6_3\underline{cm} \oplus P6_3cm$ |
| $P3\underline{c}$ | $P6_3\underline{cm} \oplus P6_3\underline{c}m$ |
| $P3c$ | $P6_3\underline{cm} \oplus P6_3cm$ |

$^a$ See Ref. 50. The $\oplus$ indicates that the tensor components of the two structures connected by it are allowed simultaneously.
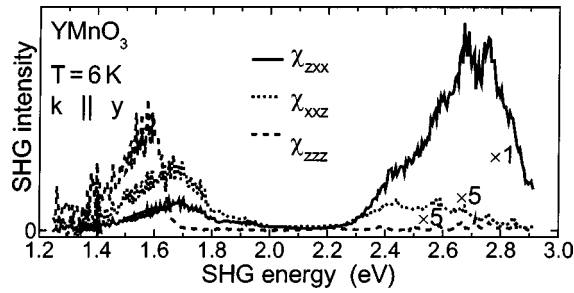
Fig. 10. *i*-type crystallographic SHG spectra of $YMnO_3$ measured at 6 K. The direction of the incident light was parallel to the $y$ axis of the crystal ($k \| y$).



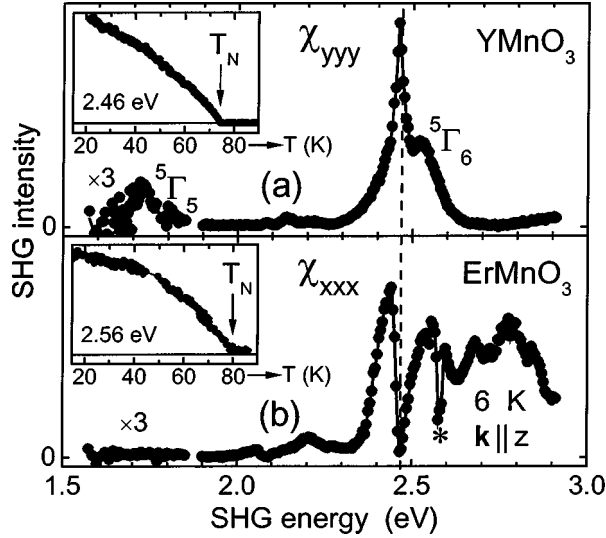Fig. 11. Magnetic SHG spectra and temperature dependence of SHG in $YMnO_3$ and $ErMnO_3$ with light incident along the $z$ axes ($k \| z$). A sharp dip marked $*$ is due to the absorption by the fundamental beam in the $^4I_{11/2}$ lines of the $Er^{3+}$ ion. The dashed line points out the correspondence between the maximum of the $\chi_{yyy}^{(c)}$ spectrum and the minimum of the $\chi_{yyy}^{(i)}$ spectrum at 2.46 eV.

comparison with the $\chi_{xxz}^{(i)}$ and $\chi_{zzz}^{(i)}$ components. The strong bands at 1.74 and 2.70 eV in the $\chi_{zxx}^{(i)}$ spectrum can be assigned to the $^5\Gamma_1(^5\Gamma_1) \rightarrow {}^5\Gamma_1(^5\Gamma_5)$ and the $^5\Gamma_1(^5\Gamma_1) \rightarrow {}^5\Gamma_1(^5\Gamma_6)$ transitions in Fig. 8(d), respectively, because these transitions are allowed both as one- and two-photon ED transitions. In turn, the slightly lower lying weak bands in the $\chi_{xxz}^{(i)}$ and $\chi_{zzz}^{(i)}$ spectra have to be assigned to the $^5\Gamma_1(^5\Gamma_1) \rightarrow {}^5\Gamma_2(^5\Gamma_5)$ and the $^5\Gamma_1(^5\Gamma_1) \rightarrow {}^5\Gamma_2(^5\Gamma_6)$ transitions, respectively. Although these transitions are ED forbidden, SHG is observed owing to admixtures from other wave functions as a result of the low local symmetry of the $Mn^{3+}$ ion.

Figure 11 shows the magnetic SHG spectra of $YMnO_3$ and $ErMnO_3$ in the 1.5–2.9-eV spectral range. In $YMnO_3$ the SHG spectrum is observed for the $\chi_{yyy}^{(c)}$ component of the nonlinear susceptibility tensor both for the high-energy transition with a peak at 2.46 eV and for the much weaker low-energy transition at 1.74 eV. The magnetic SHG spectrum of $ErMnO_3$ is observed only for the $\chi_{xxx}^{(c)}$ component of the SHG tensor, and no SHG intensity could be detected in the region of the low-energy transition. The strongest SHG signal is observed at 2.42 eV,

whereas the SHG intensity drops almost to zero at 2.46 eV, where, on the other hand, the SHG signal has a maximum value in $YMnO_3$. There is a strong broad SHG band in the region of 2.5–2.8 eV, where the SHG signal in $YMnO_3$ vanishes. Just as in the case of the crystalline SHG contributions, the resonances in the 1.5–1.7-eV range and in the 2.4–2.8-eV range can be assigned to transitions between the $^5\Gamma_1(^5\Gamma_1)$ ground state and the $^5\Gamma_1(^5\Gamma_5)$ and $^5\Gamma_1(^5\Gamma_6)$ excited states, respectively. The inset in Fig. 11 shows that the SHG signal vanishes at $T_N$, which confirms its relation to the antiferromagnetic order parameter. The analysis of the temperature dependence of the antiferromagnetic signal below $T_N$ on the basis of the power law $I^{AFM}(2\omega) \propto (1 - T/T_c)^{2\beta}$ reveals $\beta = 0.38 \pm 0.02$ as critical exponent of the antiferromagnetic order parameter. The spectra in Figs. 10 and 11 are universal to the hexagonal manganites. Although a phase with $P\underline{6}_3$ symmetry and $0° < \varphi_{spin} < 90°$ was observed for R = Sc, Ho, Lu, new spectral components to SHG were not detected. Instead, the spectra in Fig. 11 were observed simultaneously with mutually perpendicular polarization of the corresponding SHG light.

## 5. Discussion and Microscopical Models
A microscopic theory of SHG spectra in hexagonal manganites $RMnO_3$ was developed by two groups.[142,143] A single-ion approach that is supplemented by an exciton theory[143] explains the spectral dependence of $\chi_{yyy}^{(c)}$ and $\chi_{xxx}^{(c)}$ with good qualitative agreement with experimental data. For the low-energy band around 1.6 eV the relation $\chi_{yyy}^{(c)} \propto \langle S_z \rangle$ was derived, where $\langle S_z \rangle$ is an averaged $z$ component of the $Mn^{3+}$ spins. This prediction agrees with the observation of SHG spectra of $\chi_{yyy}^{(c)}$ type in $YMnO_3$, where a weak antiferromagnetic $z$ component of the $Mn^{3+}$ moments does not lower the magnetic symmetry $P\underline{6}_3 c\underline{m}$. In contrast, weak antiferromagnetism or ferromagnetism is forbidden in $ErMnO_3$. Consequently, SHG from $\chi_{xxx}^{(c)} = 0$ was not observed at 1.6 eV.

## 6. Magnetic Field Dependence
Figure 12 shows the SHG intensity's dependence on a magnetic field $H \| z$ for an $YbMnO_3$ crystal that was cooled to 6 K in zero magnetic field. Between 1.5 and 3.0 T the SHG intensity gradually decreases to zero over the whole investigated spectral range and does not recover upon field removal or reversal. This points to a transition from B-type to A-type ordering of the $Mn^{3+}$ spins, since for A-type ordering no magnetic SHG signal is allowed for light incident along the hexagonal axis. In spite of the SHG signal's being quenched, distinction between $A_1$-type and $A_2$-type ordering is possible on the basis of the spin-rotation occurring in the process of the magnetic reorientation[76] and reveals that the structure encountered by the magnetic reorientation is of the $A_2$ type. Figure 12(b) explains the presence of the $B_2 \rightarrow A_2$ transition of the $Mn^{3+}$ sublattice in $YbMnO_3$. It shows the Faraday rotation ($\Phi_F$) in $YbMnO_3$ at 1.4 K for a magnetic field $H \| z$. The rotation consists of a linear contribution $\Phi_F(H) \propto H$ from the applied field and a hysteresis $\propto M(H)$ that is due to an Ising-like magnetization of the Yb sublattices along $z$. The slopes near 0 and at 2.3 T correspond to formation of a, respectively, ferrimagnetic

and ferromagnetic single-domain state of the two $Yb^{3+}$ sublattices. A calculation of the Mn–O–Yb superexchange contributions reveals that a large magnetoelectric effect, which is allowed for A-type ordering but forbidden for B-type structures, lowers the ground-state energy, which is the reason for the $B_2 \rightarrow A_2$ transition in applied magnetic[144] (or electric[129]) fields.

Figure 13 shows the magnetic phase diagram of the hexagonal $RMnO_3$ compounds. In zero magnetic field all compounds exhibit B-type antiferromagnetic ordering with a clear correlation between the Néel temperature and the in-plane lattice constant. Upon a temperature decrease the small in-plane anisotropy leads to in-phase spin rotation and phase coexistence. Below 5 K and in applied magnetic fields $H\|z$, B → A transitions with a broad hysteresis and ferrimagnetic, ferromagnetic, or antiferromagnetic $R^{3+}$ ordering are observed for those compounds with partially filled $4f$ shell.

## 7.  Antiferromagnetic Domain Structure

In Fig. 14 the spatially resolved SHG light at 2.46 eV reveals the ferroelectric and antiferromagnetic domain structures. Dark and bright regions correspond to domains with opposite orientation of the order parameter $\mathbf{P}_S$ or $\mathbf{l}$. The ferroelectric domain structure was imaged by interference of the SHG signal wave from $\chi_{zyy}(\mathbf{P}_S)$ with a planar reference light field. Since regions with $\pm\mathbf{P}_S$ differ by 180° in the phase of the signal wave, the interference with the reference field can be constructive or destructive, which leads to the different brightness of opposite domains.[98,99] In a similar way the antiferromagnetic domain structure was imaged by interference of
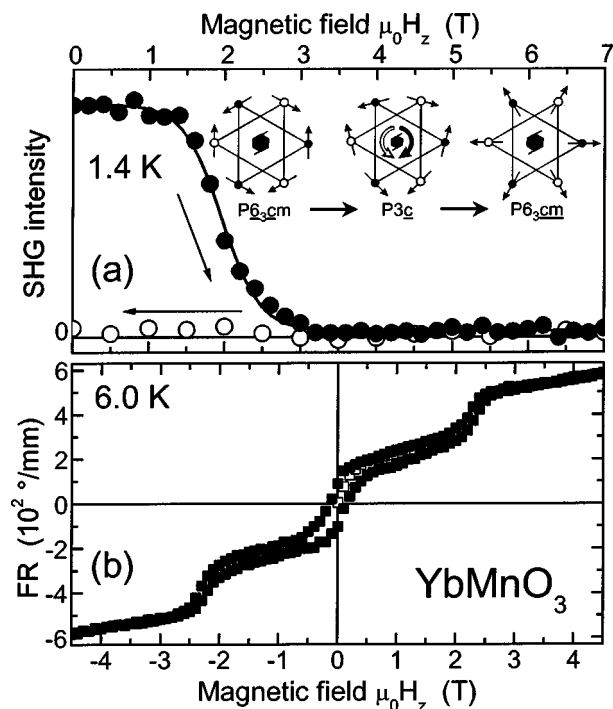


Fig. 12. Dependence on a magnetic field applied along the $z$ axis of (a) SHG intensity at 2.44 eV and (b) Faraday rotation (FR) at 1.23 eV of $YbMnO_3$. The inset in (a) depicts the rotation of $Mn^{3+}$ spins occuring in the 1.5–3.0 T interval in the field-increasing run.
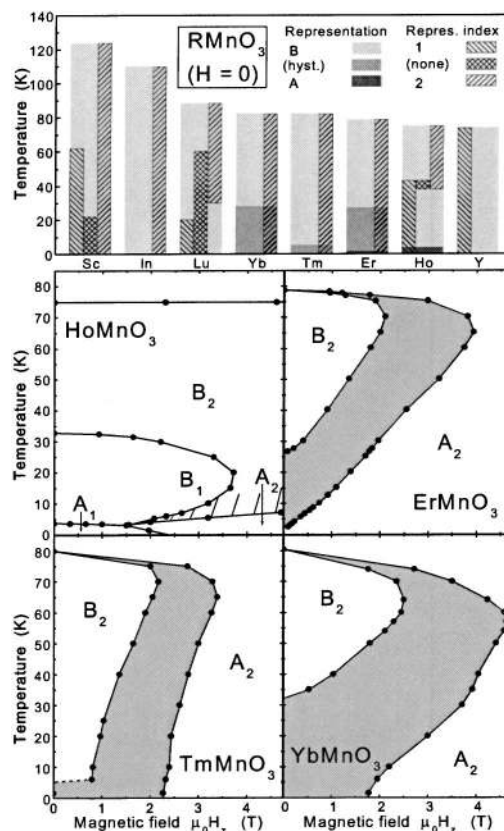


Fig. 13. Magnetic phase diagram of hexagonal $RMnO_3$. Top, magnetic phases of the $Mn^{3+}$ sublattice at zero magnetic field, increasing the in-plane lattice constant of the components from left to right; hyst., hysteresis. Lower four panels, phase diagrams of the compounds with partially filled $4f$ shell in the magnetic-field–temperature plane. The right (left) border of the gray area marks the field at which the B → A (A → B) transition in field-increasing (-decreasing) runs occurs, with the gray area representing the hysteresis. The hatched area in the $HoMnO_3$ panel indicates the presence of a very broad hysteresis.
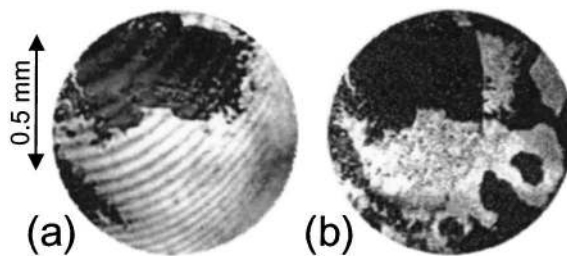


Fig. 14. Coexisting (a) ferroelectric and (b) antiferromagnetic domains in $YMnO_3$ exposed to SHG light at 2.46 eV.

the SHG waves from $\chi_{yyy}(\mathbf{P}_S\mathbf{l})$ and $\chi_{zyy}(\mathbf{P}_S)$. Depending on the orientation of $\mathbf{l}$, the interference is constructive or destructive, this time leading to a different brightness for opposite antiferromagnetic domains. The comparison between Figs. 14(a) and 14(b) shows that any reversal of the ferroelectric order parameter is accompanied by a simultaneous reversal of the antiferromagnetic order parameter. Consequently two types of antiferromagnetic domain wall are found in Fig. 14(b): clamped walls at any location of a ferroelectric domain walls in Fig. 14(a), and additional free walls within one ferroelectric domain.

The clamping cannot originate in a bulk coupling between $\mathbf{P}_S$ and $\mathbf{l}$, since a linear magnetoelectric coupling is forbidden in $YMnO_3$. However, it was shown that piezomagnetic interaction between strain induced in the ferroelectric domain walls and the magnetization inherent to the antiferromagnetic domain walls explains our observation.[145] The size of the free domains was found to be controllable by temperature annealing. A cycle through $T > T_N$ with $T \gg T_N$ produces domains with a lateral size of 1–10 $\mu$m, whereas for $T \approx T_N$ domains with a lateral size of 0.1–1 mm are observed.[146]

### B. Noncentrosymmetric Magnetic Garnet Films
Magnetic bulk garnets and garnet films are two well-known groups of materials characterized by very useful magnetic, acoustic, optical, and magneto-optical properties.[147–150] For more than four decades they have constituted one of the most actively studied groups of magnetic dielectrics.

*1. Crystallographic and Magnetic Structure*
The prototype magnetic garnet material for both bulk crystals and thin films is yttrium iron garnet, $\{Y\}_3[Fe]_2(Fe)_3O_{12}$ (YIG). The rare-earth ions $R^{3+}$ enter 24c dodecahedral positions $8\{...\}_3$, and the $Fe^{3+}$ ions enter 16a octahedral 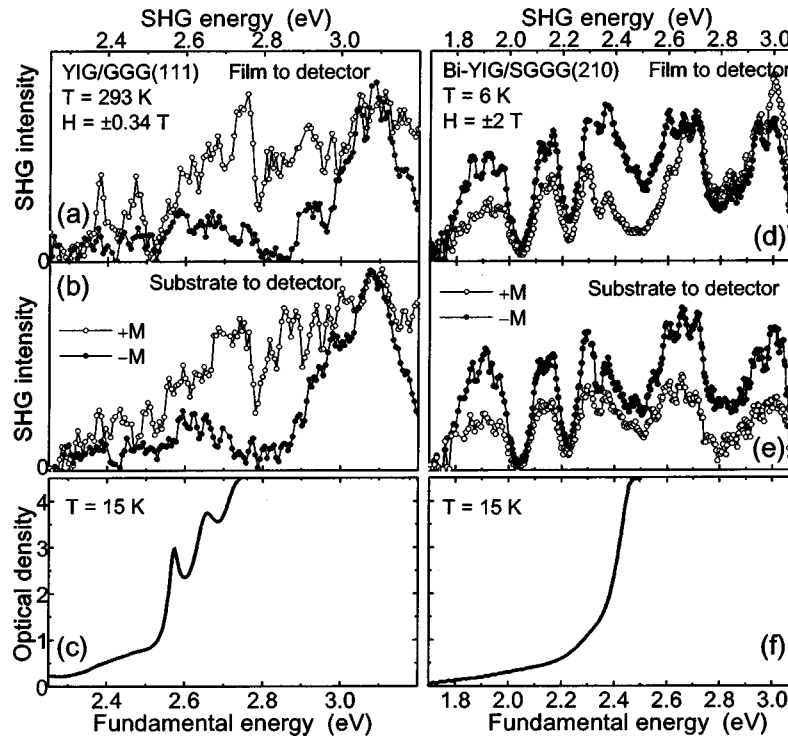positions $8[...]_2$ and 24d tetrahedral positions $8(...)_3$. Bulk crystals belong to the centrosymmetric cubic point group $m3m$ (space group $Ia3d$). However, in thin films observation of the linear magnetoelectric effect proved the breaking of centrosymmetry.[63–65] SHG in magnetic garnet films pro-

vides unambiguous proof that the crystal structure of films is noncentrosymmetric and noncubic.[30,66,67,151]

*2. Electronic Structure and Linear Optical Properties*
The magnetic iron garnets are transparent in the range 0.2–1.0 eV.[152] Above 1.0 eV absorption increases progressively because of the intrinsic localized electronic transitions between the $Fe^{3+}(3d)^5$ levels. Above 3.2 eV a further increase of absorption occurs owing to charge-transfer and interband transitions, finally approaching values up to $5 \times 10^5$ cm$^{-1}$ above 5 eV.[153] Garnets, and in particular, bismuth-substituted garnets, attracted a lot of interest because of the very large Faraday rotation of up to $10^5$ deg/cm at room temperature.

Optical absorption and reflection spectra of concentrated and diluted iron garnets are summarized in Ref. 150. In spite of the large number of publications, the assignments of spectral features are ambiguous because of the complexity of the spectra. Experimental data and crystal field calculations are summarized in Fig. 15. In its middle part Fig. 15 shows transitions in YIG that are in agreement with those reported in several papers.[152–160] The electronic structure of iron garnets has been a subject of calculations based on crystal field theory and molecular orbital theory.[152,155,159,161–163] Figure 15 shows the localized states of the $Fe^{3+}$ ions in the tetrahedral and octahedral sublattices. The derivation takes tetragonal distortions in the tetrahedral sublattice and trigonal distortions in the octahedral sublattice into account.[163] Below the bandgap the electronic transitions could be studied by op-



Fig. 15. Left two columns, crystal-field energy states of the $Fe^{3+}$ ion in the distorted tetrahedral and octahedral positions in the garnet structure.[164] Middle column, experimentally observed electronic transitions and the continuous absorption at higher photon energy. Right-hand columns, energy range of the pump beam and that of the second- and third-harmonic (THG) spectra.[170,172]

Fig. 16. SHG spectra of (a), (b) YIG/GGG(111) and (d), (e) Bi-YIG/SGGG(210) films obtained for two opposite orientations of the magnetization **M** in transverse geometry; (c), (f) corresponding linear absorption spectra.[169,171]

tical transmission methods, whereas for transitions above the charge-transfer gap reflection methods are in general more favorable.[153,154,156,157]

Optical absorption of YIG begins at ~1.2 eV and is due to the localized electronic transition $^6A_{1g} \rightarrow {}^4T_{1g}$ between the $Fe^{3+}(3d)^5$ levels in the octahedral sublattice.[155] Figure 15 shows that at higher energy the transitions in the octahedral and tetrahedral sublattices are overlapping, which complicates the assignment of states. Aside from their dependence on crystal field parameters the positions of electronic levels are subject to parameters like interatomic interaction parameters, spin–orbit coupling, exchange interaction, etc. In strongly correlated systems such as iron garnets, paired transitions (as, e.g., around 2.5 eV) may lead to additional absorption bands.

The bandgap is usually assumed to lie near 3.2–3.4 eV.[153] Substitution of $Bi^{3+}$ for $Y^{3+}$ in iron garnets leads to a shift of the absorption edge to lower energy and to a huge increase of magneto-optical effects in the visible and ultraviolet spectral range. The enhancement is assigned to an increase of spin–orbit interaction owing to formation of a molecular orbit between the $3d$ orbitals of $Fe^{3+}$ and the $2p$ orbitals of $O^{2-}$. Further mixing occurs with the $6p$ orbitals of $Bi^{3+}$, which has a large spin–orbit interaction coefficient. According to recent analysis, electronic transitions at 2.6, 3.15, and 3.9 eV dominate the Faraday rotation in bismuth-substituted garnets.[164]

### 3. Phenomenology of SHG

In magnetic garnet films the relation between the induced polarization $\mathbf{P}(2\omega)$ and the electric field $\mathbf{E}(\omega)$ of the fundamental beam and the spontaneous magnetization $\mathbf{M}(0)$ can be written as

$$\mathbf{P}(2\omega) = \epsilon_0(\chi:\mathbf{E}(\omega)\mathbf{E}(\omega) + \beta:\mathbf{E}(\omega)\mathbf{E}(\omega)\mathbf{M}(0)), \quad (15)$$

where the crystallographic and magnetic contributions are described by the polar tensor $\chi$ and the axial tensor $\beta$ [see Eq. (8)], respectively. In the ED approximation, tensors $\chi$ and $\beta$ are allowed only in noncentrosymmetric media. Nonzero components of $\chi$ and $\beta$ are determined by the crystallographic point group and given in Ref. 68. The SHG intensity is given by[98]

$$I(2\omega) \propto [|\chi|^2 + |\beta M(0)|^2 \pm 2|\chi||\beta|M(0)\cos\varphi]E^4(\omega), \quad (16)$$

where $\varphi$ is the phase difference between the SHG waves of crystallographic and magnetic origin with $\pm$ referring to opposite orientations of **M**. As in the case of $Cr_2O_3$, interference in Eq. (16) leads to different brightness in oppositely magnetized regions. Magnetization-induced SHG in garnet films was studied in several works.[165–171] Nonlinear optical rotation of SHG light was observed in one-dimensional magnetophotonic microcavities.[172]

### 4. Spectroscopy and Anisotropy

Subsequent to experiments with no[30,66,67,151] or limited[61,68,165–168] variation of photon energy we investigated SHG spectra of epitaxial magnetic garnet films in the range 1.7–3.2 eV.[169,171] Figures 16(a) and 16(b) show SHG spectra of a YIG/GGG(111) film in transverse geometry. Different spectra are obtained when SHG is emitted directly from the free film surface (film to detector) or from the surface of the film attached to the substrate (substrate to detector). In particular, a split transition near 2.4 eV is well resolved for the free film surface and smeared out for the strained surface attached to the sub-

strate.    The high magnetic visibility of the spectra was used for visualization of magnetic domain structures.[38,39,41]   According to Fig. 15, some features in the SHG spectrum can be assigned to the crystal field transitions in the two iron sublattices.   Two sharp absorption lines near 2.58 and 2.64 eV, which are presumably due to the $^6A_1 \to {}^4E$, $^4A_1$ transition in the tetrahedral sublattice and the $^6A_1 \to {}^4E$, $^4A_1$ transition in the octahedral sublattice, respectively, are also reproduced by SHG.   Further, features in the absorption spectrum at 2.9 and 3.2 eV, whose oscillator strength is an order of magnitude higher than those for the tetrahedral transitions, are visible in the SHG spectrum with the same order of magnitude as for the transitions with lower absorption.

As a rule, bismuth-substituted films show the strongest SHG signals.[68]   Figures 16(d) and 16(e) show the SHG spectra of a bismuth-substituted Bi-YIG/SGGG(210) film. A well-resolved structure with five strong bands of varying magnetic contrast is observed.   As in the case of YIG/GGG(111) films, the spectra for two sides of the film are different, and an increase of linear optical absorption does not lead to a noticeable increase of SHG intensity.

Figure 17 shows rotational anisotropies of SHG signals that were gained by projecting the component of the SHG light oriented parallel to the polarization of the incident light while rotating this polarization by 360°.   The depicted anisotropies for Bi-YIG/GGG(111) and Bi-YIG/SGGG(210) films clearly reflect the crystallographic and, by field reversal, magnetic symmetries of the surfaces. Different types of rotational anisotropy in (001), (110), (111), and (210) films were studied in Ref. 68.

### 5.   Temperature and Magnetic Field Influence on SHG in Magnetic Garnet Films

The temperature dependence of SHG in Bi-YIG/GGG(111) film is shown in Fig. 18.   The crystallographic contribution decreases linearly with temperature.   The interference term $\propto M$ shows a $(1 - T/T_C)^{0.61(6)}$ dependence, whereas the pure magnetic part $\propto BM^2$ vanishes with a $(1 - T/T_C)^{1.05(8)}$ dependence.   For the ratio between crystallographic and magnetization-induced contributions at room temperature we get $|\chi^{(c)}/\chi^{(i)}| \approx 0.4$ or
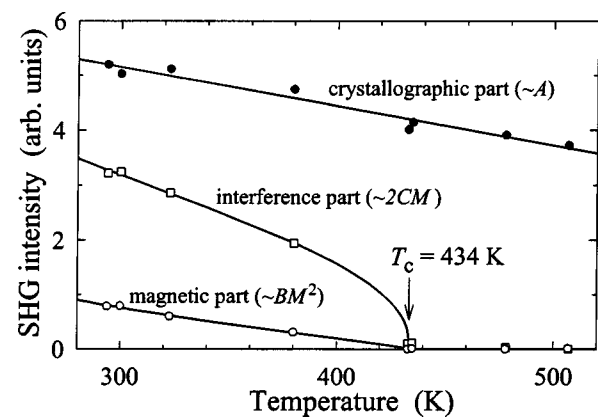


Fig. 18.   Temperature variation of crystallographic, magnetization-induced, and interference terms of the SHG intensity of the Bi-YIG/GGG(111) film.[61]

$I^{(c)}/I^{(i)} \approx 0.16$.   The dependence of magnetic SHG on the applied magnetic field is shown in Fig. 19 for a Bi-YIG/SGGG(210) film.

## 6.   SHG IN NONCENTROSYMMETRIC CRYSTALLOGRAPHIC STRUCTURES WITH NONCENTROSYMMETRIC MAGNETIC ORDER

### A.   Pyroelectric Antiferromagnet $CuB_2O_4$

In recent experiments copper metaborate was found to be a model system for nonlinear magneto-optics because it displays the complete variety of different types of magnetic SHG as defined in Section 2.   The compound will therefore be discussed in detail in this section.

### 1.   Crystallographic, Electronic, and Magnetic Structure

$CuB_2O_4$ belongs to the class of noncentrosymmetric crystals in which SHG due to charge and spin ordering is allowed.   Recently this class of materials attracted a lot of attention because of an unusual coexistence of weak Dzyaloshinskii–Moriya type ferromagnetism and inhomogeneous (incommensurate) magnetic ordering.[173,174] $CuB_2O_4$ crystallizes in the tetragonal space group $I\bar{4}2d$.[175]   Figure 20(a) shows that $Cu^{2+}$ ions are found at 4b and 8d sites with fourfold and sixfold coordination, re-
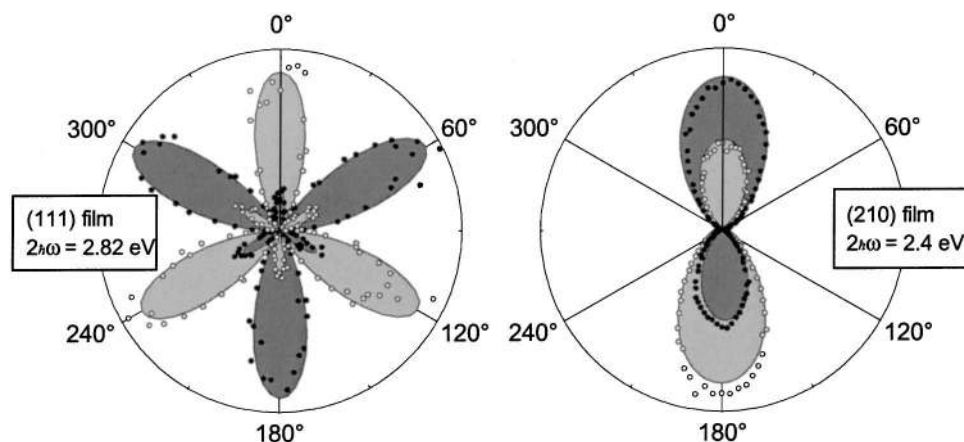


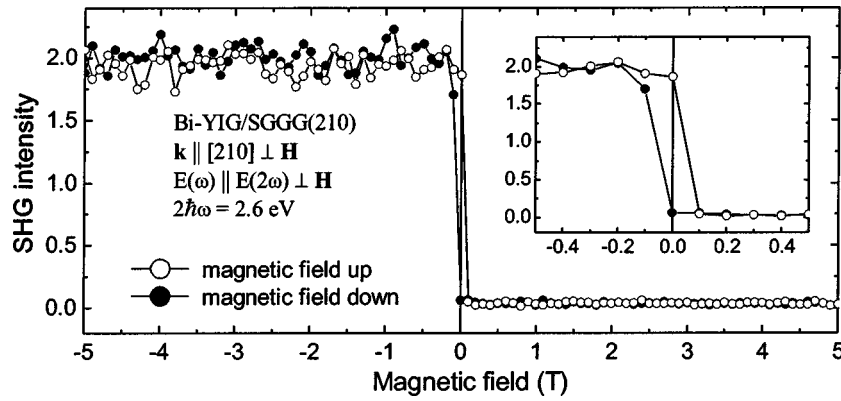Fig. 17.   Rotational anisotropies of SHG for Bi-YIG/GGG(111) and Bi-YIG/SGGG(210) films.[171]

Fig. 19.   Magnetic-field dependence of the magnetization-induced contribution to SHG for the Bi-YIG/SGGG(210) film.
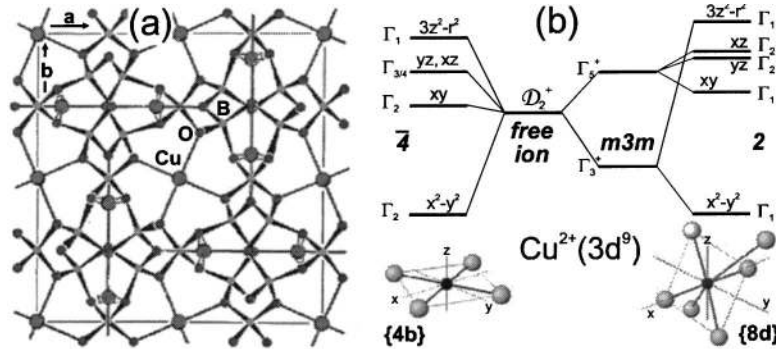


Fig. 20.   (a) Projection of the crystal structure of $CuB_2O_4$ into the plane perpendicular to the tetragonal axis.   (b) Electronic states, local symmetry, and coordination of $Cu^{2+}(3d^9)$ ions at 4b and 8d sites in $CuB_2O_4$.   Wave functions are given in terms of the local coordinate system whose axes are defined by the connections between the central $Cu^{2+}$ ion and the square or undistorted octahedron of $O^{2-}$ ligands at the respective sites.   Local symmetry is given in bold italics.   Coordination is shown for the $Cu^{2+}$ ion (black spheres) with the nearest $O^{2-}$ ligands (gray spheres).   Axes are those of the global coordinate system.

spectively.   Assuming that (i) the energy of these states scales with the degree of overlap between the wave functions of the $Cu^{2+}$ ions and their $O^{2-}$ ligands and that (ii) the influence of the remote apical $O^{2-}$ ions is small, the energy levels of the $Cu^{2+}$ ions in Fig. 20(b) are derived from the eigenstates of the free $Cu^{2+}(3d^9)$ ion.   The original $Cu^{2+}$ d-wave functions are mixed with (parity breaking) $O^{2-}$ p-wave functions because of the broken centrosymmetry.   The absence of the apical oxygen ions on the 4b positions requires the $\Gamma_1(3z^2 - r^2)$ state to have the highest energy.[176,177]   Above $T_N = 21 K$, $CuB_2O_4$ is paramagnetic.   In the range 10–21 K commensurate easy-plane antiferromagnetism with a weak Dzyaloshinskii–Moriya-type ferromagnetic component is present in the 4b sublattice.   Below 10 K the magnetic structure in zero field becomes incommensurate along the tetragonal axis.[174,178,179]   According to contemporary belief, long-range ordering at the 8d site does not occur. Magnetic frustration implies complicated magnetic structures that necessitate the use of simplified models for the interpretation of diffraction data and thus yield ambiguities in the proposed magnetic structure.[174,178,179]

*2.   Linear Optical Absorption and SHG Spectroscopy*
Figures 21 and 22 show SHG and absorption spectra of a (010) cut $CuB_2O_4$ sample for various polarizations of the incoming and outgoing light waves.   The inset in Fig.

21(b) shows that in the magnetic field the SHG intensity increases from 1 at $H = 0$ (1 defining the detection limit) by at least 3 orders of magnitude, allowing naked-eye observation at $\mu_0 H_x = 7$ T.   Therefore, according to Fig. 23(d), this A-type MFISH signal exceeds the only reported effect[57,58] by many orders of magnitude.   The MFISH spectrum displays sets of narrow lines ($<1$ meV) corresponding to transitions of the $Cu^{2+}$ ions between the electronic levels shown in Fig. 20.   This is quite unusual for wide-gap transition-metal oxides.[180–182]   The lines are accompanied by phonon-assisted transitions, forming a broadband ($>100$ meV) background.

Comparison of the MFISH spectra from $\sigma_{xxxx}$, $\sigma_{zxxx}$, and $\sigma_{zzzx}$ [with $\chi = \sigma:\mathbf{H}(0)$ as in Eq. (10)] reveals three different sets of zero-phonon transitions.[56]   We observe (i) lines at 1.410, 1.675, and 1.910 eV; (ii) lines at 1.575, 1.875, and 2.120 eV; and (iii) a line at 2.820 eV.   Set (i) is associated with transitions at the 4b site.   They are reproduced by the $\sigma_{xxxx}$ and $\sigma_{zxxx}$ components and by $\alpha$- and $\sigma$-polarized light in absorption.   Set (ii) is associated with transitions at the 8d site.   They are reproduced by the $\sigma_{zzzx}$ and $\sigma_{zxxx}$ components and by light with any polarization in absorption.   Set (iii) contains a sole line at twice the photon energy of the 1.410 eV line from set (i). This line originates in a type of two-photon transition that is enhanced by a resonant single-photon transition to the state at 1.410 eV and is discussed in Section 7.

### 3. Magnetic Structure

Observation of SHG light from $\sigma_{xxxx}$, $\sigma_{\underline{z}xxx}$, and $\sigma_{zzzx}$ is allowed in the magnetic point groups 1, $\bar{1}$, $\underline{2}$, m, $\underline{2}/m$, and eight trigonal or hexagonal groups.[50] The latter are not compatible with the crystallographic lattice, and groups $\underline{1}$ and $\underline{2}/m$ do not allow a ferromagnetic moment. Excluding monoclinic symmetry, only groups 2 and m remain. Group m points to a magnetic structure with twofold [110] axis and ferromagnetic moment parallel to this axis, whereas group $\underline{2}$ points to a magnetic structure with mirror plane [100], [010], or [001] and in-plane ferromagnetic moment. Figure 23 and the ensuing discussion show that the ferromagnetic moment can be oriented along the $x$ or $z$ axis by an external 50-mT field without further reduction of magnetic symmetry. This leaves $\underline{2}$ as the magnetic symmetry with the mirror plane perpendicular to $y$ and the magnetic moment in the $xz$ plane.

Using the lines at 1.410 and 1.875 eV, respectively, as probes for the 4b and 8d sites shows the dependence of the SHG signal on temperature and magnetic field (Fig. 23). For the 4b site the MFISH intensity at $10\,\mathrm{K} < T < 21\,\mathrm{K}$ is saturated by a 50-mT field, which points out the weak ferromagnetic moment accompanying antiferromagnetic order in this phase as its origin. For the 8d site, however, the line at 1.875 eV indicates both ferromagnetic and paramagnetic behavior, depending on the respective choice of $x$ or $z$ as the detected polarization of the MFISH signal. Obviously the $Cu^{2+}$ ions at 4b sites impose their magnetic order onto $Cu^{2+}$ ions at 8d sites, where the magnetic order coexists with a disordered para-
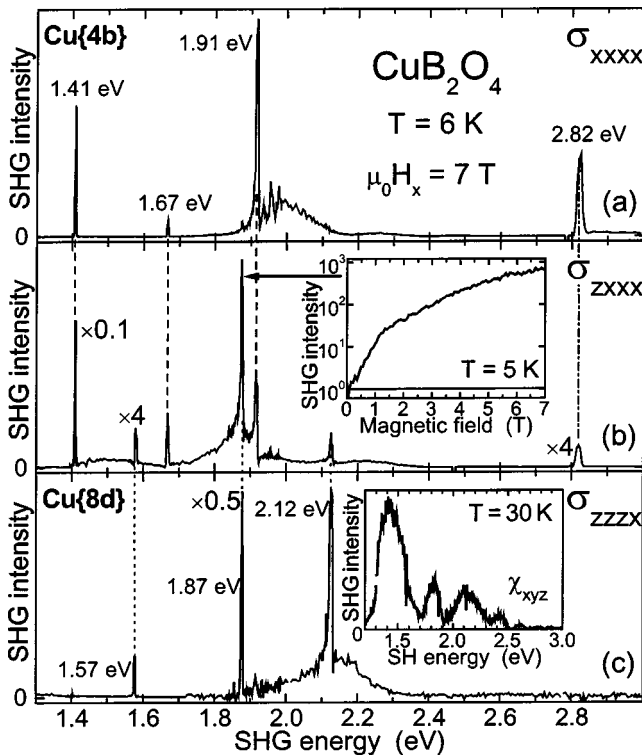


Fig. 22. Linear absorption spectra of (top) (100)-oriented and (middle, bottom) (010)-oriented $CuB_2O_4$ at $H = 0$. **k** and **E** denote the wave vector and polarization of the incoming light wave.



Fig. 23. Temperature dependence of SHG intensity at (a), (b) 4b and (c), (d) 8d sites in static magnetic fields applied along the $z$ axis of (010)-oriented $CuB_2O_4$. The inset in (b) shows the temperature dependence of linear absorption for $k\|y$, $E\|x$.



Fig. 21. Magnetic-field-induced SHG spectra of (010)-oriented $CuB_2O_4$ in a static magnetic field applied along the $x$ axis. Insets show (b) the magnetic field dependence of SHG and (c) the spectral dependence of crystallographic SHG for a (110)-oriented sample.
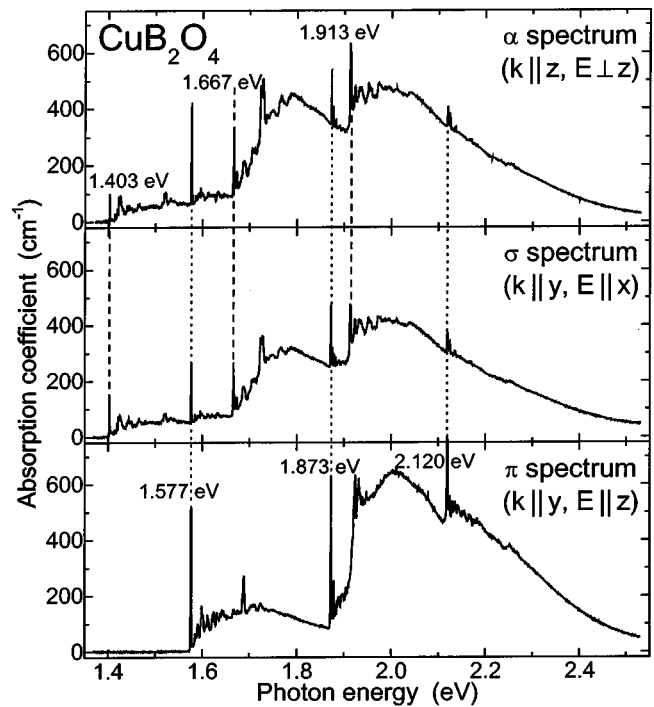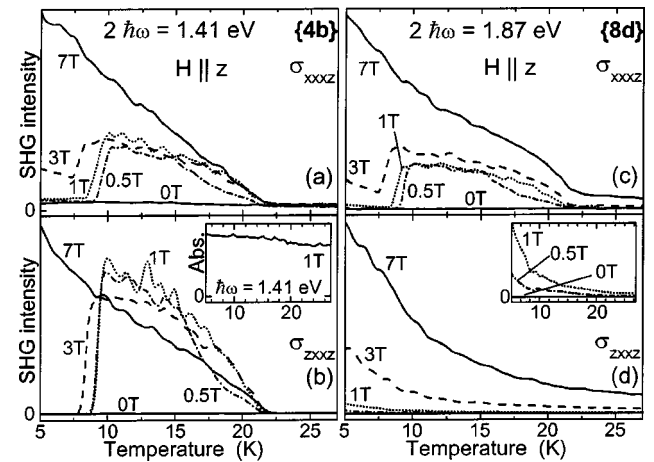
magnetic component. Contrary to contemporary belief,[174,179,183,184] the 4b and 8d sublattices are therefore strongly coupled even above 10 K.

At $\mu_0 H \leq 1$ T only A- and C-type MFISH are observed. The applied field mainly acts as catalyst, enhancing the intensity of the SHG signal probing the magnetic structure. New SHG contributions with a different polarization, which would point to a reduction of magnetic symmetry, are not observed. However, at $\mu_0 H > 1$ T Fig. 23 shows B-type MFISH from field-induced phase transitions, which are summarized in the phase diagrams in Fig. 24 for $H \perp z$ and $H \| z$. In magnetic field the incom-

mensurate purely antiferromagnetic phase is engulfed by the weakly ferromagnetic commensurate phase. At 0 K quenching occurs at the extrapolated field $\mu_0 H_x$ = 1.3 T (I → II) or $\mu_0 H_z$ = 30 T (I → III), the transitions being, respectively, of second or first order with gradual or abrupt reorientation of spins in the increasing field (see insets).

## 7. SHG IN CENTROSYMMETRIC CRYSTALLOGRAPHIC STRUCTURES WITH CENTROSYMMETRIC MAGNETIC ORDER

Until now we restricted ourselves to discussion of systems with at least one noncentrosymmetric subsystem, allowing a treatment within the ED approximation. Since most magnetically ordered compounds are centrosymmetric, we conclude our review by demonstrating that the potential of SHG remains almost unimpaired by the restrictions on SHG from the point of view of behavior under the spatial inversion operation.

### A. Centrosymmetric Antiferromagnets NiO and CoO

Recently an increased interest in antiferromagnets for practical applications was triggered by the development of spin-valve devices as a basis for magnetic read heads. One of the most promising compounds in this sense is NiO, which combines a simple crystallographic structure with the technically advantageous high Néel temperature of 523 K. It is further expected that SHG can give valuable information about the magnetic excitations and spin dynamics in this compound down to the femtosecond time scale.[185,186] We therefore discuss novel methods for SHG in centrosymmetric compounds, using NiO and CoO as examples.

### 1. Crystallographic and Magnetic Structure

NiO and CoO crystallize in the cubic rock-salt structure (point group $m3m$).[187] The electronic structure of, in particular, NiO was subject to intensive

experimental[187–189] and theoretical[187,190–193] studies. Below $T_N$ = 523 K the $Ni^{2+}$ spins are ordered ferromagnetically in {111} planes, where they lie along $\langle 11\bar{2} \rangle$ axes.[194,195] The sign of the ferromagnetic order is reversed in adjacent {111} planes, which establishes the antiferromagnetic order and leads to four types of T domain, corresponding to the four $\langle 111 \rangle$ axes. The T domains are contracted along the $\langle 111 \rangle$ axes,[196] which reduces the symmetry to $\bar{3}m$. To each T domain six types of S domain with three possible orientations of spins within the {111} planes are associated.[194,196] In CoO the $Co^{2+}$ ions are ordered antiferromagnetically below $T_N$ = 292 K, pointing along the $\langle 117 \rangle$ axes.[197] This leads to three types of T-domain for which a small tetragonal distortion reduces the symmetry to $4/mmm$. In both compounds small distortions along the spin direction further reduce the symmetry, but the crystals remain centrosymmetric.[198]

### 2. Resonance-Enhanced MD SHG

Figures 25 and 26 show the SHG and linear absorption spectra of NiO and CoO. In spite of inversion symmetry, SHG with distinct spectral features is observed. NiO exhibits a doublet of sharp lines. In CoO this doublet is less pronounced but nevertheless present. The comparison with the absorption spectra reveals that the SHG signal projects the electronic transitions of the fundamental wave at the energy $\hbar\omega$ on the intensity dependence of the SHG wave at the energy $2\hbar\omega$ rather than reproducing the excitation of the electronic states at $2\hbar\omega$. Temperature-dependent measurement of the SHG intensity show that all signals vanish at $T_N$, which confirms their magnetic origin. Note that, in contrast to previous examples, coupling to the SHG field is quadratic in $\mathbf{l}$ and thus is related to magnetostrictive lattice distortions.[46]

According to relations (1)–(3) and Ref. 46, MD SHG of the type

$$\mathbf{P}(\mathbf{2}\omega) \propto \hat{\chi}^{eem}(-2\omega;\ \omega,\ \omega)\mathbf{E}(\omega)\mathbf{H}(\omega) \qquad (17)$$

is compatible with the observed SHG signal. Other contributions, and among them especially those that are of
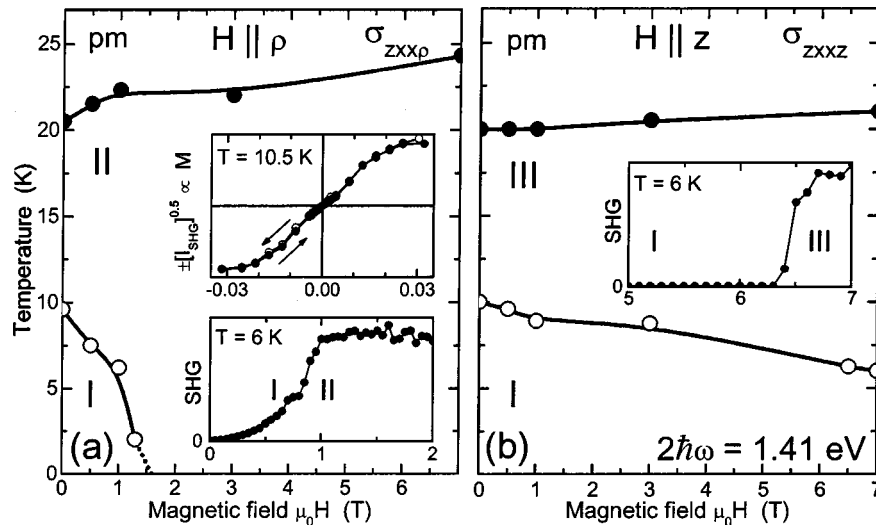


Fig. 24. Phase diagrams of $CuB_2O_4$ in the magnetic-field–temperature plane for (a) in-plane ($H\|\rho$ with $\rho = x + y$) and (b) uniaxial ($H\|z$) magnetic field. Insets, SHG intensity $I_{SHG}$ or magnetization $M \propto \pm I_{SHG}^{0.5}$ dependence on the magnetic field for selected points in the phase diagram.
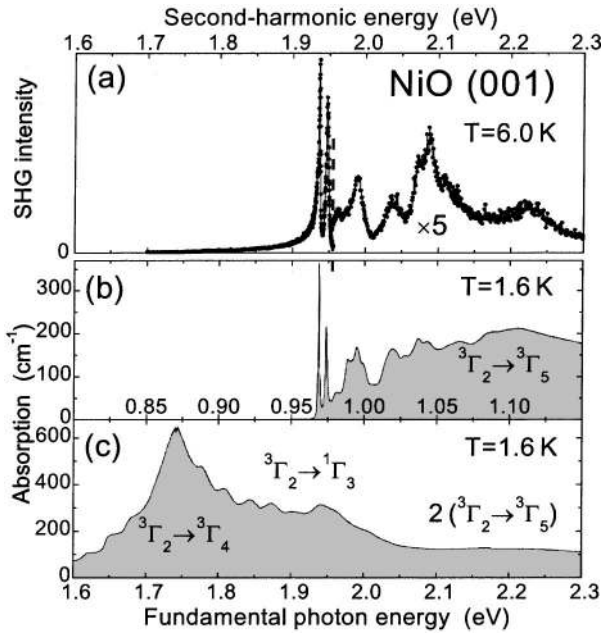
Fig. 25.   (a) SHG spectra and (b), (c) linear absorption spectra of a multidomain (001)-oriented NiO crystal in the region of the lowest $(3d)^8$ single-ion transitions.   The spectra were gained with linearly polarized incident light.
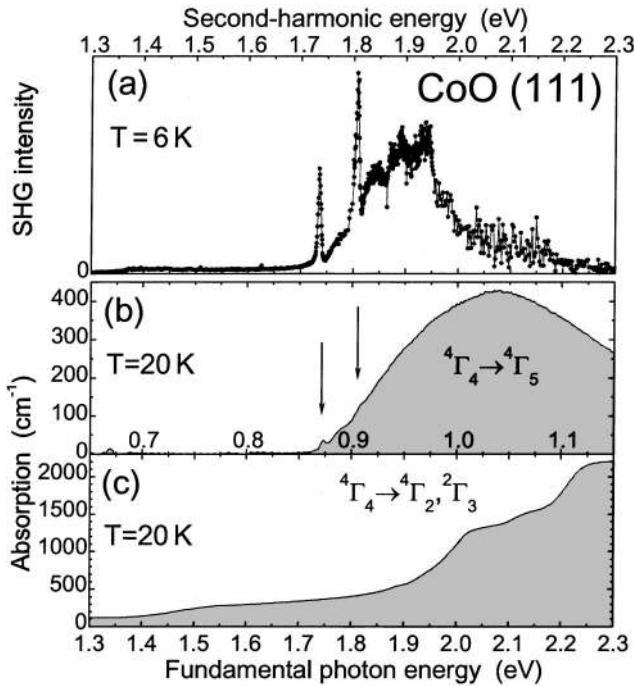


Fig. 26.   (a) SHG spectra and (b), (c) linear absorption spectra of a multidomain (111)-oriented CoO crystal in the region of the lowest $(3d)^7$ single-ion transitions.   The spectra were gained with linearly polarized incident light.   Vertical arrows indicate the position of narrow lines in the slope of the $^4\Gamma_4 \rightarrow {}^4\Gamma_5$ peak.

the same order of magnitude in the multipole expansion of the light field as the process in relation (17), can be excluded on the basis of their different selection rules.   The microscopic expression for the nonlinear optical susceptibility $\hat{\chi}^{eem}$ can be written as[6,13,92,93]

$$\chi_{ijk}^{eem} \propto \sum_{g,n,n'} \left[ \frac{(P_i)_{gn}(P_j)_{nn'}(M_k)_{n'g}}{(2\omega - \omega_{ng})(\omega - \omega_{n'g})} + \cdots \right] p_g^{(0)},$$

$$(18)$$

where $\hbar\omega_{ng}$ and $\hbar\omega_{n'g}$ refer to the energy difference for the transfer from the ground state $|g\rangle$ to the excited state $|n\rangle$ and the intermediate state $|n'\rangle$, respectively.   $M_k$ and $P_{i,j}$ are the vector components of the MD and ED moment operators, respectively; $p_g^{(0)}$ describes the thermal distribution in the ground-state multiplet.

Although in the multipole expansion of the light field the MD contribution is 2 orders of magnitude weaker than the ED contribution, relation (18) shows that this ratio can be counterbalanced if the two-photon transition is resonant not only at the SHG frequency $2\omega$ but also for the absorption of the first photon at the frequency $\omega$. Figure 27 shows that for $Ni^{2+}(3d^8)$ and $Co^{2+}(3d^7)$ intermediate levels between the ground state and the excited state can contribute to such twofold resonance enhancement.   Therefore the distinct sequence of transitions at the energy of the fundamental wave dominates the SHG spectrum and leads to its peculiar single-photon-like spectral dependence.   In NiO the narrow lines correspond to the transition from the lowest $^3\Gamma_2$ substate to the two lowest $^3\Gamma_5$ substates of the $Ni^{2+}(3d^8)$ after taking into account spin–orbit and exchange interactions.[46]   In CoO a transition to the $^2\Gamma_3$ or $^2\Gamma_4$ level of the $^2G$ orbital may also contribute to the doublet.   MnO does not display any detectable SHG signal below $T_N$ because for $Mn^{2+}(3d)^5$ no intermediate states exist at the energy of the single-photon transition.

*3.  Distinction between Antiferromagnetic Domains*
Figure 28 shows the anisotropy of the SHG signal that was gained from different regions of (111)-oriented NiO and CoO samples by projecting the component of the SHG light oriented parallel to the polarization of the incident light while rotating this polarization by 360°.   If the signal from the whole sample with a statistical distribution of domains is integrated, a sixfold symmetry is observed that reflects the symmetry of the paramagnetic crystal.   Whereas the SHG intensity in NiO drops to zero every
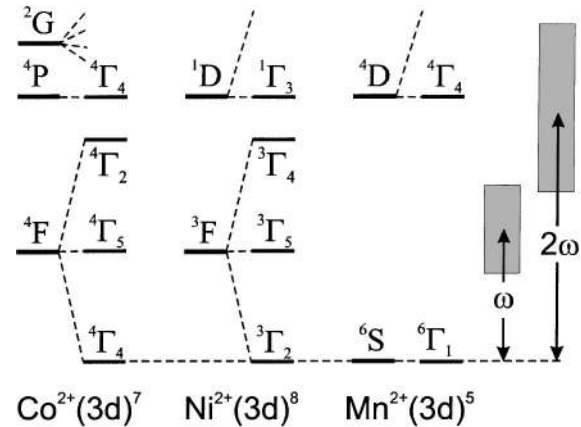


Fig. 27.   Schematic splitting of the Hund-coupled orbitals of the free $Co^{2+}$, $Ni^{2+}$, and $Mn^{2+}$ ions in the octahedral crystal field. The SHG process with excitation at energies $\hbar\omega$ and $2\hbar\omega$ is indicated by the arrows.
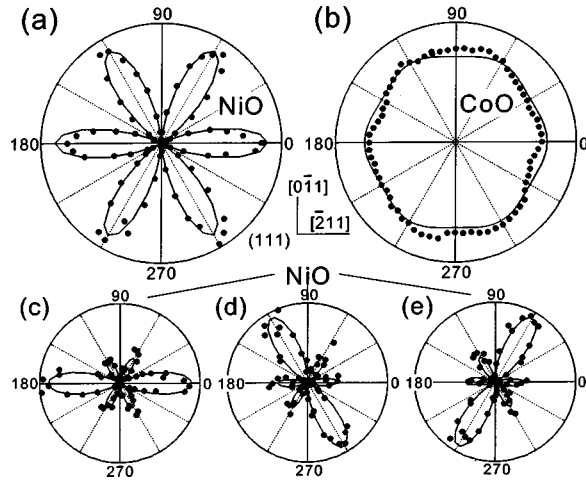
Fig. 28. (a), (b) Anisotropy of the SHG intensity from multidomain regions of a NiO and a CoO sample. (c), (d), (e) Anisotropy for three different regions of a (111)-oriented T domain in NiO. The polarization dependence of the SHG signal reveals the three differently oriented S domains. Solid curves, fits of the nonzero tensor components $\chi_{ijk}^{eem}$ to the data. The center of each polar diagram corresponds to zero SHG intensity.
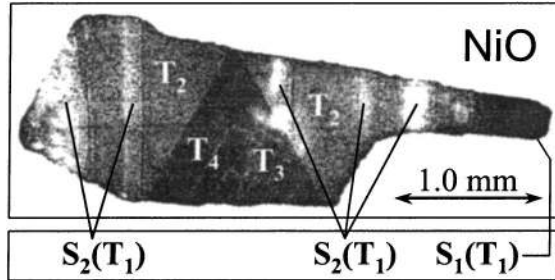


Fig. 29. S and T domains in NiO taken with SHG light at 2.05 eV. Incident fundamental and detected SHG light is polarized along the $[01\bar{1}]$ axis.

60°, the polarization dependence in CoO is almost isotropic. This reflects the different orientation of the $Ni^{2+}$ and $Co^{2+}$ spins, which corresponds to different magnetic symmetries with a different set of components $\chi_{ijk}^{eem} \neq 0$ in relation (17). Figures 28(c)–28(e) show the polarization dependence of SHG on a single (111)-oriented T domain. SHG clearly distinguishes three different regions in which the maximum intensity is observed with light polarized along the $(\bar{2}11)$, the $(1\bar{2}1)$, or the $(11\bar{2})$ axis. The twofold rotational anisotropy of the SHG signal and the 120° shifts between the polarization diagrams show that the three regions correspond to the different S domains inside the T domain. The contrast between the S domains is as high as 3:1, whereas it is hardly noticeable in a linear optical experiment.[199] Only opposite 180° domains that differ in the sign of the antiferromagnetic order parameter **l** cannot be distinguished by SHG owing to the quadratic coupling to **l**.

Figure 29 shows the image of a (111) oriented sample obtained by SHG in transmission. Before the experiment, four types of T domains could be identified by linear birefringence. Although in a linear transmission experiment no difference is observed between the regions assigned to T domain 1, a distinct difference in the brightness of the SHG signal is obvious and points to different

types of S domains within T domain 1. Again, the nonlinear experiment can reveal important information about the details of the magnetic structure that are imperceptible by linear optics.

## 8. CONCLUSIONS

Spectroscopic SHG experiments in magnetically ordered dielectrics show that nonlinear magneto-optics is a powerful complement to existing techniques for the investigation of magnetic symmetries, structures, and interactions. The simplest example is SHG in the ED approximation, which is expressed by the equation $P_i(2\omega) = \epsilon_0 \chi_{ijk} E_j(\omega) E_k(\omega)$. According to the von Neumann principle the components $\chi_{ijk}$ of the nonlinear susceptibility are determined by the magnetocrystalline symmetry. Crystallographic and magnetic contributions to SHG can be separated on the basis of their different spectral and polarization dependence. In the present case ED SHG was applied for the investigation of various compounds with noncentrosymmetric crystallographic or magnetic structure, such as $Cr_2O_3$, hexagonal manganites, thin garnet films, and $CuB_2O_4$. Contributions of higher order than ED SHG were employed for investigation of systems with a center of inversion. For example, MD SHG with enhanced efficiency because of the involvement of multiple resonant electronic transitions was introduced with antiferromagnetic NiO and CoO as model systems.

The relative amplitude of magnetic contributions in comparison with the nonmagnetic background exceeds that of linear optical experiments by several orders of magnitude. In the case of antiferromagnets, linear optical phenomena coupling to a macroscopic magnetization fail entirely, so that nonlinear optical techniques become especially useful. Consequent use of spectroscopy and topography as characteristic degrees of freedom of optical experiments revealed novel and, in many cases, surprising results. It was shown that for a solitary crystal structure a broad variety of magnetic structures with subtle differences were distinguished with a high degree of discrimination. Hidden phase transitions in frustrated compounds and sublattice interaction in systems with multiple-order parameters were visualized. Interface contributions to magnetic order in thin garnet films were identified. Magnetic phase diagrams were established for all hexagonal manganites, a long-standing task until the introduction of magnetic SHG. In spatially resolved measurements antiferromagnetic 180° domains were observed in $Cr_2O_3$ in a few minutes with high contrast and diffraction-limited spatial resolution. With an experimental setup for the determination of both amplitude and phase of a SHG wave, several unexpected phenomena were revealed for the system of hexagonal manganites. A possibility for controlling the size of antiferromagnetic domains through annealing above the Néel temperature was found. An interaction of antiferromagnetic and ferroelectric domains at their walls, which represents a higher-order magnetoelectric effect in nonmagnetoelectric materials, was observed and theoretically explained on the basis of piezomagnetic interaction. S domains were distinguished in NiO.

We believe that the possibilities of nonlinear optical spectroscopy in general and SHG spectroscopy in particular are far from being fully explored.  In this review we discussed only a few specific examples that demonstrate the high potential of SHG for the study of known and unknown physical phenomena in magnetic materials.  Undoubtedly SHG can be applied to many other magnetic dielectrics, semiconductors, and metals with few requirements for the crystallographic and magnetic symmetry.  Besides that, future experiments on nonlinear magneto-optics will undoubtedly focus on systematic exploitation of the temporal degree of freedom in optical pump-and-probe experiments on magnetically ordered systems, and, in particular, antiferromagnets, in continuation of introductory experiments reported in Refs. 9 and 200.

## ACKNOWLEDGMENTS

## REFERENCES AND NOTES

1. P. A. Franken, A. E. Hill, C. W. Peters, and G. Weinreich, "Generation of optical harmonics," Phys. Rev. Lett. **7**, 118–119 (1961).
2. S. A. Akhmanov and R. V. Khokhlov, *Problems of Nonlinear Optics* (Vserossiisky Institut Nauchnoi i Tekhnicheskoi Informatsii, Moscow, 1964) (in Russian).
3. N. Bloembergen, *Nonlinear Optics* (Benjamin, New York, 1965).
4. S. A. Akhmanov and N. I. Koroteev, *Methods of Nonlinear Optics and Spectroscopy of the Light Diffusion* (Nauka, Moscow, 1981) (in Russian).
5. D. N. Klyshko, *Photons and Nonlinear Optics* (Nauka, Moscow, 1980) (in Russian).
6. Y. R. Shen, *The Principles of Nonlinear Optics* (Wiley, New York, 1984).
7. R. W. Boyd, *Nonlinear Optics* (Academic, London, 1992).
8. P. N. Butcher and D. Cotter, *The Elements of Nonlinear Optics* (Cambridge U. Press, Cambridge, UK, 1990).
9. K. H. Bennemann, ed., *Nonlinear Optics in Metals* (Clarendon, Oxford, UK, 1998).
10. P. S. Pershan, "Nonlinear optical properties of solids: energy considerations," Phys. Rev. **130**, 919–929 (1963).
11. E. Adler, "Nonlinear optical frequency polarization in a dielectric," Phys. Rev. **134**, A728–A733 (1964).
12. J. Lajzerowicz and M. Vallade, "Génération du second harmonique dans les substances magnétiques ordonnées," C. R. Seances Acad. Sci., Ser. B **264**, 1819–1821 (1967).
13. S. Kielich and R. Zawodny, "Optical nonlinear phenomena in magnetized crystals and isotropic bodies," Acta Phys. Pol. A **43**, 579–603 (1973).
14. S. Kielich and R. Zawodny, "On new nonlinear magneto-optical phenomena in crystals and liquids," Opt. Acta **20**, 867–877 (1973).
15. N. N. Akhmediev, S. B. Borisov, A. K. Zvezdin, I. L. Lyubchanski, and Yu. V. Melikhov, "Nonlinear optical susceptibility of magnetically ordered crystals," Sov. Phys. Solid State **27**, 650–652 (1985).
16. S. B. Borisov and I. L. Lyubchanskii, "Microscopic theory of the nonlinear optical susceptibility of magnetics," Opt. Spectrosc. **61**, 801–804 (1986).
17. S. S. Girgel and T. V. Demidova, "Frequency conversion of electromagnetic waves in crystals with a centrosymmetric paramagnetic phase," Opt. Spectrosc. **62**, 63–65 (1987).
18. R.-P. Pan and Y. R. Shen, "Optical second harmonic generation as a probe for surface magnetization," Chin. J. Phys. (Taipei) **25**, 175–177 (1987).
19. R.-P. Pan, H. D. Wei, and Y. R. Shen, "Optical second-harmonic generation from magnetized surfaces," Phys. Rev. B **39**, 1229–1234 (1989).
20. W. Hübner and K. H. Bennemann, "Nonlinear magneto-optical Kerr effect on a nickel surface," Phys. Rev. B **40**, 5973–5979 (1989).
21. J. Kociński, "The nonlinear optical susceptibility tensor $\xi_{ijk}$ in a diperiodic magnetic layer," J. Magn. Magn. Mater. **104–107**, 1787–1788 (1992).
22. R. Zawodny, "Nonlinear magneto-optics of magnetically ordered crystals," Adv. Chem. Phys. **85**, 307–374 (1993).
23. A. K. Zvesdin, "Non-linear surface Kerr effect and SHG in magnets," Physica A **241**, 444–449 (1997).
24. A. K. Zvezdin and N. F. Kubrakov, "Nonlinear magneto-optical Kerr effects," JETP **89**, 77–85 (1999).
25. V. I. Belotelov, A. P. Pyatakov, S. A. Eremin, G. G. Musaev, and A. K. Zvezdin, "New nonlinear intensity Kerr effect in the polar geometry," Phys. Solid State **42**, 1873–1880 (2000).
26. V. I. Belotelov, A. P. Pyatakov, G. G. Musaev, S. A. Eremin, and A. K. Zvezdin, "Nonlinear intensity-related magneto-optical Kerr effects in the planar geometry," Opt. Spectrosc. **91**, 626–633 (2001).
27. A. M. Agaltsov, V. S. Gorelik, A. K. Zvezdin, V. A. Murashov, and D. N. Rakov, "Temperature dependence of the second harmonic generation in ferroelectric-magnetic bismuth ferrite," Sov. Phys. Short Commun. **5**, 37–39 (1989).
28. V. A. Murashov, D. N. Rakov, V. M. Ionov, I. S. Dubenko, Y. V. Titov, and V. S. Gorelik, "Magnetoelectric (Bi, Ln)FeO$_3$ compounds: crystal growth, structure and properties," Ferroelectrics **162**, 11–21 (1994).
29. R. V. Pisarev, "Crystal optics of magnetoelectrics," Ferroelectrics **162**, 191–209 (1994).
30. O. A. Aktsipetrov, O. V. Braginskii, and D. A. Esikov, "Nonlinear optics of gyrotropyc media: second harmonic generation in rare-earth iron garnets," Sov. J. Quantum Electron. **20**, 259–263 (1990).
31. J. Reif, J. C. Zink, C.-M. Schneider, and J. Kirschner, "Effects of surface magnetism on optical second harmonic generation," Phys. Rev. Lett. **67**, 2878–2881 (1991).
32. J. Reif, C. Rau, and E. Matthias, "Influence of magnetism on second harmonic generation," Phys. Rev. Lett. **71**, 1931–1934 (1993).
33. E. Matthias and F. Träger, eds., *Proceedings of the Topical Conference: Nonlinear Optics at Interfaces (NOPTI 1998)*, Appl. Phys. B **68** (1999).
34. F. Träger, ed., *Proceedings of the Topical Conference: Nonlinear Optics at Interfaces (NOPTI 2001)*, Appl. Phys. B **74** (2002).
35. Th. Rasing, "Nonlinear magneto-optics," J. Magn. Magn. Mater. **175**, 35–50 (1997).
36. O. A. Aktsipetrov, "Nonlinear magneto-optics in magnetic nanoparticles," Colloids Surf., A **202**, 165–173 (2002).
37. A. Kirilyuk, "Nonlinear optics in application to magnetic surfaces and thin films," J. Phys. D **35**, R189–R207 (2002).
38. A. Kirilyuk, V. Kirilyuk, Th. Rasing, V. V. Pavlov, and R. V. Pisarev, "Domain and domain wall images by second harmonic generation," J. Magn. Soc. Jpn. **20(S1)**, 361–364 (1996).
39. A. Kirilyuk, V. Kirilyuk, and Th. Rasing, "A combined nonlinear and linear magneto-optical microscopy," Appl. Phys. Lett. **70**, 2306–2308 (1997).
40. I. I. Smolyaninov, A. V. Zayats, and C. C. Davis, "Near-field second-harmonic imaging of ferromagnetic and ferroelectric materials," Opt. Lett. **22**, 1592–1594 (1997).
41. D. Wegner, U. Conrad, J. Güdde, G. Meyer, T. Crecelius, and A. Bauer, "In-plane magnetization of garnet films imaged by proximal probe nonlinear magneto-optical microscopy," J. Appl. Phys. **88**, 2166–2168 (2000).
42. V. V. Pavlov, J. Ferré, P. Meyer, G. Tessier, P. Georges, A.

Brun, P. Beauvillain, and V. Mathet, "Linear and non-linear magneto-optical studies of Pt/Co/Pt thin films," J. Phys.: Condens. Matter **13**, 9867–9878 (2001).

43. J. Hohlfeld, E. Matthias, R. Knorren, and K. H. Bennemann, "Nonequilibrium magnetization dynamics of nickel," Phys. Rev. Lett. **78**, 4861–4864 (1997).

44. B. Koopmans, M. van Kampen, J. T. Kohlhepp, and W. J. M. de Jonge, "Ultrafast magneto-optics in nickel: magnetism or optics?" Phys. Rev. Lett. **85**, 844–847 (2000).

45. H. Regensburger, R. Vollmer, and J. Kirschner, "Time-resolved magnetization-induced second-harmonic generation from the Ni(110) surface," Phys. Rev. B **61**, 14716–14722 (2000).

46. M. Fiebig, D. Fröhlich, B. B. Krichevtsov, and R. V. Pisarev, "Second harmonic generation and magnetic-dipole-electric-dipole interference in antiferromagnetic $Cr_2O_3$," Phys. Rev. Lett. **73**, 2127–2130 (1994).

47. A. K. Zvezdin and V. A. Kotov, *Modern Magnetooptics and Magnetooptical Materials* (IOP, Bristol, 1997).

48. S. Sugano and N. Kojima, eds., *Magneto-Optics* (Springer-Verlag, Berlin, 2000).

49. T. H. O'Dell, *The Electrodynamics of Magnetoelectric Media* (North-Holland, Amsterdam, 1970).

50. R. R. Birss, *Symmetry and Magnetism* (North-Holland, Amsterdam, 1966).

51. M. Trzeciecki and W. Hübner, "Time-reversal symmetry in nonlinear optics," Phys. Rev. B **62**, 13888–13891 (2000).

52. D. Sa, R. Valentí, and C. Gros, "A generalized Ginzburg–Landau approach to second harmonic generation," Eur. Phys. J. B **14**, 301–305 (2000).

53. C. H. Lee, R. K. Chang, and N. Bloembergen, "Nonlinear electroreflectance in silicon and silver," Phys. Rev. Lett. **18**, 167–170 (1967).

54. M. M. Fejer, G. A. Magel, D. H. Jundt, and R. L. Byer, "Quasi-phase-matched second harmonic generation: tuning and tolerances," IEEE J. Quantum Electron. **28**, 2631–2654 (1992).

55. R. W. Terhune, P. D. Maker, and C. M. Savage, "Optical harmonic generation in calcite," Phys. Rev. Lett. **8**, 404–406 (1962).

56. R. V. Pisarev, I. Sänger, G. A. Petrakovskii, and M. Fiebig, "Magnetic-field induced second harmonic generation in $CuB_2O_4$," Phys. Rev. Lett. **93**, 037204/1–4 (2004).

57. T. Suzuki, V. Venkataramanan, and M. Aono, "Magnetic-field-induced second-harmonic generation on Si(111)-7 × 7," Jpn. J. Appl. Phys., Part 1 **40**, L1119–L1122 (2001).

58. V. Venkataramanan, K. Noguchi, M. Aono, and T. Suzuki, "A sensitive detection method for magnetization-induced second-harmonic generation under an externally applied field," Appl. Phys. B: Photophys. Laser Chem. **74**, 683–689 (2002).

59. J. Ferré, "Linear and non-linear magneto-optical effects," in *Magnetism and Synchrotron Radiation*, E. Beaurepaire, F. Scheurer, G. Krill, and J. P. Kappler, eds. (Springer-Verlag, Heidelberg, 2001), pp. 316–335.

60. D. N. Astrov, "The magnetoelectric effect in antiferromagnetics," Sov. Phys. JETP **11**, 708–709 (1960).

61. V. V. Pavlov, R. V. Pisarev, A. Kirilyuk, and Th. Rasing, "Observation of a transversal nonlinear magneto-optical effect in thin magnetic garnet films," Phys. Rev. Lett. **78**, 2004–2007 (1997).

62. Y. Ogawa, Y. Kaneko, J. P. He, X. Z. Yu, T. Arima, and Y. Tokura, "Magnetization-induced second harmonic generation in a polar ferromagnet," Phys. Rev. Lett. **92**, 047401/1–4 (2004).

63. B. B. Krichevtsov, V. V. Pavlov, and R. V. Pisarev, "Giant linear magnetoelectric effect in garnet ferrite films," JETP Lett. **49**, 535–539 (1989).

64. B. B. Krichevtsov, V. V. Pavlov, and R. V. Pisarev, "Linear effects of an electric field on the magnetization processes in iron garnet films," Phys. Solid State **31**, 1142–1148 (1989).

65. B. B. Krichevtsov, V. V. Pavlov, R. V. Pisarev, and A. G. Selitsky, "Linear magnetoelectric effect in magnetic garnet thin films," Ferroelectrics **161**, 65–71 (1994).

66. R. V. Pisarev, B. B. Krichevtsov, V. N. Gridnev, V. P. Klin, D.

67. Fröhlich, and Ch. Pahlke-Lerch, "Optical second-harmonic generation in magnetic garnet thin films," J. Phys.: Condens. Matter **5**, 8621–8628 (1993).

67. G. Petrocelli, S. Martellucci, and M. Richetta, "Bismuth induced enhancement of the second-harmonic generation efficiency in bismuth-substituted yttrium iron garnet films," Appl. Phys. Lett. **63**, 3402–3404 (1993).

68. V. N. Gridnev, V. V. Pavlov, and R. V. Pisarev, "Second harmonic generation in anisotropic magnetic films," Phys. Rev. B **63**, 184407/1–11 (2001).

69. D. Fröhlich, St. Leute, V. V. Pavlov, R. V. Pisarev, A. Kirilyuk, and Th. Reasing, "Nonlinear optical spectroscopy of the two-order-parameter compound $YMnO_3$," Phys. Rev. Lett. **81**, 3239–3242 (1998).

70. M. Fiebig, D. Fröhlich, K. Kohn, St. Leute, Th. Lottermoser, V. V. Pavlov, and R. V. Pisarev, "Determination of the magnetic symmetry of hexagonal manganites by second harmonic generation," Phys. Rev. Lett. **84**, 5620–5623 (2000).

71. C. Degenhardt, M. Fiebig, D. Fröhlich, Th. Lottermoser, and R. V. Pisarev, "Nonlinear optical spectroscopy of electronic transitions in hexagonal manganites," Appl. Phys. B: Lasers Opt. **73**, 139–144 (2001).

72. M. Fiebig, Th. Lottermoser, D. Fröhlich, A. V. Goltsev, and R. V. Pisarev, "Observation of coupled magnetic and electric domains," Nature (London) **419**, 818–820 (2002).

73. R. Pauthenet and C. Veyret, "Les propriétés magnétostatiques des manganites de terres rares," J. Phys. (Paris) **31**, 65 (1970). Curie temperatures were incorrectly listed owing to a misprint.

74. N. Iwata and K. Kohn, "Dielectric anomalies at magnetic transitions of hexagonal rare earth manganese oxides $RMnO_3$," J. Phys. Soc. Jpn. **67**, 3318–3319 (1998). The results for $ErMnO_3$ and $HoMnO_3$ have to be exchanged.

75. H. Sugie, N. Iwata, and K. Kohn, "Magnetic ordering of rare earth ions and magnetic-electric interaction of hexagonal $RMnO_3$ (R = Ho, Er, Yb or Lu)," J. Phys. Soc. Jpn. **71**, 1558–1564 (2002).

76. M. Fiebig, Th. Lottermoser, and R. V. Pisarev, "Spin-rotation phenomena and magnetic phase diagrams of hexagonal $RMnO_3$," J. Appl. Phys. **93**, 8194–8196 (2003).

77. A. Muñoz, J. A. Alonso, M. J. Martínez-Lope, M. T. Casáis, J. L. Martínez, and M. T. Fernández-Díaz, "Evolution of the magnetic structure of hexagonal $HoMnO_3$ from neutron powder diffraction data," Chem. Mater. **13**, 1497–1505 (2001).

78. Th. Lonkai, D. Hohlwein, J. Ihringer, and W. Prandl, "The magnetic structures of $YMnO_{3-\delta}$ and $HoMnO_3$," Appl. Phys. A: Mater. Sci. Process. **74**, S843–S845 (2002).

79. S. Kielich and R. Zawodny, "DC magnetic field induced second harmonic generation of laser beam," Opt. Commun. **4**, 132 (1971).

80. J. E. Sipe, D. J. Moss, and H. M. van Driel, "Phenomenological theory of optical second- and third-harmonic generation from cubic centrosymmetric crystals," Phys. Rev. B **35**, 1129–1141 (1987).

81. J. E. Sipe, V. Mizrahi, and G. I. Stegeman, "Fundamental difficulty in the use of second-harmonic generation as a strictly surface probe," Phys. Rev. B **35**, 9091–9094 (1987).

82. P. Guyot-Sionnest and Y. R. Shen, "Bulk contribution in surface second-harmonic generation," Phys. Rev. B **38**, 7985–7989 (1988).

83. J. J. Maki, M. Kauranen, and A. Persoons, "Surface second-harmonic generation from chiral materials," Phys. Rev. B **51**, 1425–1434 (1995).

84. H. W. K. Tom, T. F. Heinz, and Y. R. Shen, "Second-harmonic reflection from silicon surfaces and its relation to structural symmetry," Phys. Rev. Lett. **51**, 1983–1986 (1983).

85. E. W. Meijer, E. E. Havinga, and G. L. J. A. Rikken, "Second-harmonic generation in centrosymmetric crystals of chiral molecules," Phys. Rev. Lett. **65**, 37–39 (1990).

86. B. Koopmans, A.-M. Janner, H. T. Jonkman, G. A. Sawatzky, and F. van der Woude, "Strong bulk magnetic dipole induced second-harmonic generation from $C_{60}$," Phys. Rev. Lett. **71**, 3569–3572 (1993).

87. Th. Verbiest, M. Kauranen, J. J. Maki, M. N. Teerenstra, A. J. Schouten, R. J. M. Nolte, and A. Persoons, "Linearly polarized probes of surface chirality," J. Chem. Phys. **103**, 8296–8298 (1995).

88. A. V. Balakin, N. I. Koroteev, A. V. Pakulev, A. P. Shkurinov, D. Boucher, P. Masselin, and E. Fertein, "Polarization characteristics of the 'forbidden' second optical harmonic of femtosecond laser pulses in a bacteriorhodopsin solution," JETP **85**, 52–60 (1997).

89. M. Fiebig, D. Fröhlich, and R. V. Pisarev, "Nonlinear spectroscopy of antiferromagnetic $Cr_2O_3$," J. Appl. Phys. **81**, 4875–4877 (1997).

90. V. N. Muthukumar, R. Valentí, and C. Gros, "Microscopic model of nonreciprocal optical effects in $Cr_2O_3$," Phys. Rev. Lett. **75**, 2766–2769 (1995).

91. V. N. Muthukumar, R. Valentí, and C. Gros, "Theory of nonreciprocal optical effects in antiferromagnets: The case of $Cr_2O_3$," Phys. Rev. B **54**, 433–440 (1996).

92. M. Muto, Yu. Tanabe, T. Iizuka-Sakano, and E. Hanamura, "Magnetoelectric and second-harmonic spectra in antiferromagnetic $Cr_2O_3$," Phys. Rev. B **57**, 9586–9607 (1998).

93. Y. Tanabe, M. Muto, M. Fiebig, and E. Hanamura, "Interference of second harmonics due to electric and magnetic dipoles in antiferromagnetic $Cr_2O_3$," Phys. Rev. B **58**, 8654–8666 (1998).

94. M. Fiebig, D. Fröhlich, Th. Lottermoser, V. V. Pavlov, R. V. Pisarev, and H.-J. Weber, "Second harmonic generation in the centrosymmetric antiferromagnet NiO," Phys. Rev. Lett. **87**, 137202/1–4 (2001).

95. M. Fiebig, Th. Lottermoser, V. V. Pavlov, and R. V. Pisarev, "Magnetic second harmonic generation in centrosymmetric CoO, NiO, and $KNiF_3$," J. Appl. Phys. **93**, 6900–6902 (2003).

96. M. Fiebig, D. Fröhlich, Th. Lottermoser, V. V. Pavlov, R. V. Pisarev, and J.-H. Weber, "Optical second harmonic generation in centrosymmetric antiferromagnetic NiO," in *XI Feofilov Symposium on Spectroscopy of Crystals Activated by Rare-Earth and Transition Metal Ions*, Proc. SPIE **4766**, 238–247 (2002).

97. M. Fiebig, D. Fröhlich, Th. Lottermoser, V. V. Pavlov, R. V. Pisarev, and H.-J. Weber, "Second harmonic generation of magnetic-dipole type in the centrosymmetric antiferromagnets NiO and $KNiF_3$," J. Magn. Magn. Mater. **258–259**, 110–113 (2003).

98. St. Leute, Th. Lottermoser, and D. Fröhlich, "Nonlinear spatially resolved phase spectroscopy," Opt. Lett. **24**, 1520–1522 (1999).

99. M. Fiebig, D. Fröhlich, T. Lottermoser, and S. Kallenbach, "Phase-resolved second-harmonic imaging with non-ideal laser sources," Opt. Lett. **29**, 41–43 (2004).

100. R. E. Newnham and Y. M. de Haan, "Refinement of the $\alpha$-$Al_2O_3$, $Ti_2O_3$, $V_2O_3$, and $Cr_2O_3$ structure," Z. Kristallogr. **117**, 235–237 (1962).

101. B. N. Brockhouse, "Antiferromagnetic structure in $Cr_2O_3$," J. Chem. Phys. **21**, 961–962 (1953).

102. Y. Tanabe and S. Sugano, "On the absorption spectra of complex ions," J. Phys. Soc. Jpn. **9**, 753–766 (1954).

103. Y. Tanabe and K. Aoyagi, "Excitons in magnetic insulators," in *Excitons*, E. I. Rashba and M. D. Sturge, eds. (North-Holland, Amsterdam, 1982), pp. 603-664.

104. J. P. van der Ziel, "Davydov splitting of the $^2E$ lines in antiferromagnetic $Cr_2O_3$," Phys. Rev. Lett. **18**, 237239 (1967).

105. D. S. McClure, "Comparison of the crystal fields and optical spectra of $Cr_2O_3$ and ruby," J. Chem. Phys. **38**, 2289–2294 (1963).

106. J. W. Allen, R. M. Macfarlane, and R. L. White, "Magnetic Davydov splitting in the optical absorption spectrum of $Cr_2O_3$," Phys. Rev. **179**, 523–541 (1969).

107. R. M. Macfarlane and J. W. Allen, "Exciton bands in antiferromagnetic $Cr_2O_3$," Phys. Rev. B **4**, 3054–3067 (1971).

108. S. I. Shablaev, I. P. Areshev, and R. V. Pisarev, "Resonant two-photon absorption in the $Cr_2O_3$ antiferromagnet," Phys. Solid State **42**, 1868–1872 (2000).

109. I. E. Dzyaloshinskii, "The magnetoelectric effect in antiferromagnetic materials," Sov. Phys. JETP **10**, 628–629 (1960).

110. L. M. Corliss and J. M. Hastings, "Magnetic structure studies at Brookhaven National Laboratory," J. Phys. (Paris) **25**, 557–562 (1964).

111. M. Fiebig, D. Fröhlich, and H.-J. Thiele, "Determination of spin direction in the spin-flop phase of $Cr_2O_3$," Phys. Rev. B **54**, 12681–12684 (1996).

112. J. Ohtani and K. Kohn, "Magnetoelectric effect and spin direction in a spin-flopped $Cr_2O_3$ single crystal," J. Phys. Soc. Jpn. **53**, 3744–3746 (1984).

113. H. Wiegelmann, A. G. M. Jansen, P. Wyder, J. P. Rivera, and H. Schmid, "Magnetoelectric effect of $Cr_2O_3$ in strong static magnetic fields," Ferroelectrics **162**, 141–146 (1994).

114. Y. F. Popov, Z. A. Kazeǐ, and A. M. Kadomtseva, "Linear magnetoelectric effect in $Cr_2O_3$ in strong magnetic fields," JETP Lett. **55**, 234–238 (1992).

115. D. V. Belov, G. P. Vorob'ev, A. M. Kadomtseva, and Y. F. Popov, "Magnetoelectric effect in the spin-flop-phase of $Cr_2O_3$ and the problem of determining the magnetic structure," JETP Lett. **58**, 579–584 (1993).

116. J. M. D. Coey, M. Viret, and S. von Molnar, "Mixed-valence manganites," Adv. Phys. **48**, 167–293 (1999).

117. H. L. Yakel, W. C. Koehler, E. F. Bertraut, and E. F. Forrat, "On crystal structure of manganese (111) trioxides of heavy lanthanides and yttrium," Acta Crystallogr. **16**, 957–963 (1963).

118. H. W. Xu, J. Iwasaki, T. Shimizu, H. Sato, and N. Kamegashira, "Structure, magnetic-susceptibility and heatcapacity of $ScMnO_3$," J. Alloys Compd. **221**, 274–279 (1995).

119. M. Bieringer and J. E. Greedan, "Magnetic structure and spin reorientation transition in $ScMnO_3$," J. Solid State Chem. **143**, 132–139 (1999).

120. A. Muñoz, J. A. Alonso, M. Y. Martínez-Lope, M. T. Casáis, J. L. Martínez, and M. T. Fernández-Díaz, "Magnetic structure of hexagonal $RMnO_3$ (R = Y, Sc): thermal evolution from neutron powder diffraction data," Phys. Rev. B **62**, 9498–9510 (2000).

121. M. N. Iliev, H. G. Lee, V. N. Popov, M. V. Abrashev, A. Hamed, R. L. Meng, and C. W. Chu, "Raman- and infrared-active phonons in hexagonal $YMnO_3$: experiment and lattice-dynamical calculations," Phys. Rev. B **56**, 2488–2494 (1997).

122. S. C. Abrahams, "Ferroelectricity and structure in the $YMnO_3$ family," Acta Crystallogr. **57**, 485–490 (2001).

123. K. Lukaszewicz and J. Karut-Kalicinska, "X-ray investigations of the crystal structure and phase transitions of $YMnO_3$," Ferroelectrics **7**, 81–82 (1974).

124. Th. Lonkai, U. Amman, J. Ihringer, D. G. Tomuta, R. W. A. Hendrikx, D. M. Többens, and J. A. Mydosh, "Development of the high-temperature phase of hexagonal manganites," Phys. Rev. B **69**, 134108/1–10 (2004).

125. B. B. Van Aken, T. T. M. Palstra, A. Filippetti, and N. A. Spaldin, "Origin of ferroelectricity in magnetoelectric $YMnO_3$," Nature Mater. **3**, 164–170 (2004).

126. E. F. Bertaut, M. Mercier, and R. Pauthenet, "Structure magnétique de $MnYO_3$," Phys. Lett. **5**, 27–29 (1963).

127. W. C. Koehler, H. L. Yakel, E. O. Wollan, and J. W. Cable, "The magnetic structure of rear-earth manganites," in *Proceedings of the 4th Conference on Rare-Earth Research* (Gordon & Breach, New York, 1965), p. 63–75.

128. Y. A. Izyumov, V. E. Naish, and R. P. Ozerov, *Neutron Diffraction of Magnetic Materials* (Plenum, New York, 1991).

129. Th. Lottermoser, Th. Lonkai, U. Amann, D. Hohlwein, J. Ihringer, and M. Fiebig, "Magnetic phase control by an electric field," Nature (London) **430**, 541–544 (2004).

130. K. Kritayakirana, P. Berger, and R. V. Jones, "Optical spectra of ferroelectric–antiferromagnetic rare earth manganates," Opt. Commun. **1**, 95–98 (1969).

131. G. H. Dieke, *Spectra and Energy Levels of Rare Earth Ions in Crystals* (Interscience, New York, 1968).

132. W.-C. Yi, S.-I. Kwun, and J.-G. Yoon, "Study on the electronic structure of hexagonal and orthorhombic $YMnO_3$," J. Phys. Soc. Jpn. **69**, 2706–2707 (2000).

133. M. Takahashi and J. Igarashi, "Local approach to electronic excitations in MnO, FeO, CoO, and NiO," Phys. Rev. B **54**, 13566–13574 (1996).

134. A. V. Kimel, R. V. Pisarev, F. Bentivegna, and Th. Rasing, "Time-resolved nonlinear optical spectroscopy of $Mn^{3+}$ ions in rare-earth hexagonal manganites $RMnO_3$ ($R$ = Sc, Y, Er)," Phys. Rev. B **64**, 201103/1–4 (2001).

135. A. B. Souchkov, J. R. Simpson, M. Quijada, H. Ishibashi, N. Hur, J. S. Ahn, S. W. Cheong, A. J. Millis, and H. D. Drewl, "Exchange interaction effects on the optical properties of $LuMnO_3$," Phys. Rev. Lett. **91**, 027203/1–4 (2003).

136. A. M. Kalashnikova and R. V. Pisarev, "Electronic structure of hexagonal rare-earth manganites $RMnO_3$," JETP Lett. **78**, 143–147 (2003).

137. R. M. A. Azzam and N. M. Bashara, *Ellipsometry and Polarized Light* (North-Holland, Amsterdam, 1977).

138. J. E. Medvedeva, V. I. Anisimov, M. A. Korotin, O. N. Mryasov, and A. J. Freeman, "The effect of Coulomb correlation and magnetic ordering on the electronic structure of two hexagonal phases of ferroelectromagnetic $YMnO_3$," J. Phys.: Condens. Matter **12**, 4947–4958 (2000).

139. M. Qian, J. Dong, and Q. Zheng, "Electronic structure of the ferroelectromagnet $YMnO_3$," Phys. Lett. A **270**, 96–101 (2000).

140. G. M. Nedlin, "Possible ordered magnetic structures of $YMnO_3$-type crystals," Sov. Phys. Solid State **6**, 2156–2161 (1965).

141. W. Sikora and V. N. Syromyatnikov, "Symmetry analysis of magnetic-structure in hexagonal manganites $ErMnO_3$, $HoMnO_3$, $LuMnO_3$, $ScMnO_3$, $TmMnO_3$, $YMnO_3$," J. Magn. Magn. Mater. **60**, 199–203 (1986).

142. X. Wan, J. Dong, M. Quian, and W. Zhang, "Nonlinear optical properties of perovskite $YMnO_3$ studied by real-space recursion method," Phys. Rev. B **61**, 10664–10669 (2000).

143. T. Iizuka-Sakano, E. Nakamura, and Y. Tanabe, "Second-harmonic-generation spectra of the hexagonal manganites $RMnO_3$," J. Phys.: Condens. Matter **13**, 3031–3055 (2001).

144. M. Fiebig, C. Degenhardt, and R. V. Pisarev, "Interaction of frustrated magnetic sublattices in $ErMnO_3$," Phys. Rev. Lett. **88**, 027203/1–4 (2002).

145. A. V. Goltsev, R. V. Pisarev, Th. Lottermoser, and M. Fiebig, "Structure and interaction of antiferromagnetic domain walls in hexagonal $YMnO_3$," Phys. Rev. Lett. **90**, 177204/1–4 (2003).

146. M. Fiebig, D. Fröhlich, S. Leute, and R. V. Pisarev, "Second harmonic spectroscopy and control of domain size in antiferromagnetic $YMnO_3$," J. Appl. Phys. **83**, 6560–6562 (1998).

147. A. Paoletti, ed., *Physics of Magnetic Garnets* (North-Holland, Amsterdam, 1978).

148. G. Winkler, *Magnetic Garnets* (Vieweg, Braunschweig, 1981).

149. A. Paoletti, ed., "Magnetic garnet films," special issue, Thin Solid Films **114** (1984).

150. H. P. J. Wijn, ed., *Magnetic Properties of Nonmetallic Inorganic Compounds Based on Transition Elements*, Vol 27/e of Landolt-Börnstein: Numerical Data and Functional Relationships in Science and Technology, New Series, Group III (Springer-Verlag, Berlin, 1991).

151. O. A. Aktsipetrov, V. A. Aleshkevich, A. V. Melnikov, T. V. Misuryaev, T. V. Murzina, and V. V. Randoshkin, "Magnetic field induced effects in optical second harmonic generation from iron garnet films," J. Magn. Magn. Mater. **165**, 421–423 (1997).

152. D. L. Wood and J. P. Remeika, "Effect of impurities on optical properties of yttriom iron garnet," J. Appl. Phys. **38**, 1038–1045 (1967).

153. G. B. Scott and J. L. Page, "Absorption spectra of $Y_3Fe_5O_{12}$ and $Y_3Ga_5O_{12}$—$Fe^{3+}$ to 5.5 eV," Phys. Status Solidi B **79**, 203–213 (1977).

154. F. J. Kahn, P. S. Pershan, and J. P. Remeika, "Ultraviolet magneto-optical properties of single-crystal orthoferrites, garnets, and other ferric oxide compounds," Phys. Rev. **186**, 891–918 (1969).

155. J. P. van der Ziel, J. F. Dillon, Jr., and J. P. Remeika, "Excitons, spin-wave sidebands, and exchange interactions in yttrium iron garnet," AIP Conf. Proc. **5**, 254–258 (1971).

156. A. I. Galuza, V. V. Eremenko, and A. P. Kirichenko, "Optical properties of yttrium-ferrite garnet," Sov. Phys. Solid State **15**, 407 (1973).

157. K. W. Blazey, "Wavelength-modulated spectra of some $Fe^{3+}$ oxides," J. Appl. Phys. **45**, 2273–2280 (1974).

158. S. H. Wemple, S. L. Blank, J. A. Seman, and W. A. Biolsi, "Optical properties of epitaxial iron garnet thin films," Phys. Rev. B **9**, 2134–2144 (1974).

159. G. B. Scott, D. E. Lacklison, and J. L. Page, "Absorption spectra of $Y_3Fe_5O_{12}$ (YIG) and $Y_3Ga_5O_{12}$:$Fe^{3+}$," Phys. Rev. B **10**, 971–986 (1974).

160. B. B. Krichevtsov, O. Ochilov, and R. V. Pisarev, "Sublattice anisotropy of the magnetic linear dichroism of yttrium-iron garnet $Y_3Fe_5O_{12}$," Phys. Solid State **25**, 1380–1385 (1983).

161. T. K. Vien, J. L. Dormann, and H. Le Gall, "Crystal-field splitting in octahedral and tetrahedral symmetry for $Fe^{3+}$ ions in $Y_3Fe_5O_{12}$," Phys. Status Solidi **71**, 731–739 (1975).

162. A. S. Moskvin, A. V. Zenkov, E. I. Yuryeva, and V. A. Gubanov, "Origin of the magneto-optical properties of iron garnets," Physica B **168**, 187–196 (1991).

163. V. V. Alekseev, V. V. Druzhinin, and R. V. Pisarev, "Analysis of the yttrium iron garnet optical spectrum with allowance for local lattice distortions," Phys. Solid State **33**, 1507–1510 (1991).

164. G. F. Dionne and G. A. Allen, "Spectral origins of giant Faraday rotation and ellipticity in Bi-substituted magnetic garnets," J. Appl. Phys. **73**, 6127–6129 (1993).

165. R. V. Pisarev, V. V. Pavlov, A. Kirilyuk, and Th. Rasing, "Nonlinear magnetooptics in garnets," J. Magn. Soc. Jpn. **20**(S1), 23–28 (1996).

166. V. V. Pavlov, R. V. Pisarev, A. Kirilyuk, and Th. Rasing, "A spectroscopic study of the nonlinear magneto-optical response of garnets," J. Appl. Phys. **81**, 4631–4633 (1997).

167. A. Kirilyuk, R. V. Pisarev, V. N. Gridnev, V. V. Pavlov, and Th. Rasing, "Nonlinear optics of magnetic crystals," J. Magn. Soc. Jpn. **23**, 346–351 (1999).

168. A. Kirilyuk, V. V. Pavlov, R. V. Pisarev, and Th. Rasing, "Asymmetry of second harmonic generation in magnetic thin films under circular optical exitation," Phys. Rev. B **61**, R3796–R3799 (2000).

169. V. V. Pavlov, R. V. Pisarev, M. Fiebig, and D. Fröhlich, "Nonlinear optical spectroscopy of epitaxial magnetic garnet films," Low Temp. Phys. **28**, 523–527 (2002).

170. V. V. Pavlov, R. V. Pisarev, M. Fiebig, D. Fröhlich, and Th. Lottermoser, "Magnetoelectric phenomena in nonlinear optics," Ferroelectrics **279**, 93–109 (2002).

171. V. V. Pavlov, R. V. Pisarev, M. Fiebig, and D. Fröhlich, "Optical harmonic generation in magnetic garnet epitaxial films near the fundamental absorption edge," Phys. Solid State **45**, 662–669 (2003).

172. A. A. Fedyanin, T. Yoshida, K. Nishimura, G. Marowsky, M. Inoue, and O. A. Aktsipetrov, "Nonlinear magneto-optical Kerr effect in gyrotropic photonic band gap structures: magneto-photonic microcavities," J. Magn. Magn. Mater. **258–259**, 96–98 (2003).

173. A. N. Bogdanov, U. K. Rößler, M. Wolf, and K. H. Müller, "Magnetic structures and reorientation transitions in noncentrosymmetric uniaxial antiferromagnets," Phys. Rev. B **66**, 214410/1–16 (2002).

174. B. Roessli, J. Schefer, G. A. Petrovskii, B. Ouladdiaf, M. Boehm, U. Staub, A. Vorotinaov, and L. Bezmaternikh, "Formation of a magnetic soliton lattice in copper metaborate," Phys. Rev. Lett. **86**, 1885–1888 (2001).

175. M. Martinez-Ripoli, S. Martinez-Carrera, and S. Garcia-Blanco, "The crystal structure of copper metaborate, $CuB_2O_4$," Acta Crystallogr., Sect. B: Struct. Crystallogr. Cryst. Chem. **27**, 677–681 (1971).

176. A. B. P. Lever, *Inorganic Electronic Spectroscopy* (Elsevier, Amsterdam, 1984).

177. R. G. Burns, *Mineralogical Applications of Crystal Field Theory* (Cambridge U. Press, Cambridge, UK, 1993).

178. G. A. Petrakovskii, A. D. Balaev, and A. M. Vorotynov, "Magnetic susceptibility and magnetic-field behavior of $CuB_2O_4$ copper metaborate," Phys. Solid State **42**, 321–325 (2000).

179. M. Boehm, S. Martynov, B. Roessli, G. Petrakovskii, and J. Kulda, "Spin-wave spectrum of copper metaborate in the commensurate phase $10\,K < T < 21\,K$," J. Magn. Magn. Mater. **250**, 313–318 (2002).

180. Y. Tokura, S. Koshihara, T. Arima, H. Takagi, S. Ishibashi, T. Ido, and S. Uchida, Phys. Rev. B **41**, 11657–11660 (1990).

181. M. Bassi, P. Camagni, R. Rolli, G. Samoggia, F. Parmigiani, G. Dhalenne, and A. Revcolevschi, "Optical absorption of $CuGeO_3$," Phys. Rev. B **54**, 11030–11033 (1996).

182. Y. Okimoto, Y. Tomioka, Y. Onose, Y. Otsuka, and Y. Tokura, "Charge ordering and disordering transitions in $Pr_{1-x}Ca_xMnO_3$ ($x = 0.4$) as investigated by optical spectroscopy," Phys. Rev. B **57**, R9377–R9380 (1998).

183. G. A. Petrakovskii, M. A. Popov, B. Roessli, and B. Ouladdiaf, "Incommensurate magnetic structure in copper metaborate," J. Exp. Theor. Phys. **93**, 809–814 (2001).

184. H. Nakamura, Y. Fujii, H. Kikuchi, and M. Chiba, "$^{11}$B-NMR in soliton lattice system $CuB_2O_4$," J. Magn. Magn. Mater. **272–276**, 1007–1008 (2004).

185. R. Gómez-Abal, O. Ney, K. Satitkovitchai, and W. Hübner, "All-optical subpicosecond magnetic switching in NiO(001)," Phys. Rev. Lett. **92**, 227402 (2004).

186. M. Trzeciecki, A. Dähn, and W. Hübner, "Symmetry analysis of second-harmonic generation at surfaces of antiferromagnets," Phys. Rev. B **60**, 1144–1160 (1999).

187. O. Madelung, ed., *Semiconductors: Physics of Nontetrahedrally Bonded Binary Compounds*, Vol. 17g of Landolt-Börnstein: Numerical Data and Functional Relationships, New Series, Group 3 (Springer-Verlag, Berlin, 1984).

188. S. Hüfner, *Photoelectron Spectroscopy*, (Springer-Verlag, Berlin, 1996).

189. B. Fromme, *d–d Excitations in Transition-Metal Oxides* (Springer-Verlag, Berlin, 2001).

190. M. Takahashi and J. Igarashi, "Local approach to electronic excitations in MnO, FeO, CoO, and NiO," Phys. Rev. B **54**, 13566–13574 (1996).

191. T. Bredow and A. R. Gerson, "Effect of exchange and correlation on bulk properties of MgO, NiO, and CoO," Phys. Rev. B **61**, 5194–5201 (2000).

192. N. A. Mironova, G. A. Grinvald, V. N. Skvortsova, and U. A. Ulmanis, "Fine-structure of anti-ferromagnetic NiO absorption spectra," Sov. Phys. Solid State **23**, 874–875 (1981).

193. T. Tsuboi and W. Kleemann, "Fine-structure of near-infrared optical-absorption in NiO," J. Phys. Condens. Matter **6**, 8625–8631 (1994).

194. M. T. Hutchings and E. J. Samuelsen, "Measurement of spin-wave dispersion in NiO by inelastic neutron-scattering and its relation to magnetic properties," Phys. Rev. B **6**, 3447–3461 (1972).

195. F. U. Hillebrecht, H. Ohldag, N. B. Weber, C. Bethke, and U. Mick, "Magnetic moments at the surface of antiferromagnetic NiO(100)," Phys. Rev. Lett. **86**, 3419–3422 (2001).

196. K. Nakahigashi, N. Fukuoka, and Y. Shimomura, "Crystal-structure of antiferromagnetic NiO determined by x-ray topography," J. Phys. Soc. Jpn. **38**, 1634–1640 (1975).

197. W. L. Roth, "Magnetic structure of MnO, FeO, CoO, and NiO," Phys. Rev. **110**, 1333–1341 (1958).

198. S. J. Joshua, *Symmetry Principles and Magnetic Symmetry in Solid State Physics* (Adam Hilger, New York, 1991).

199. W. Kleemann, F. J. Schäfer, and D. S. Tannhauser, "Linear birefringence in *S*-domains of NiO near the antiferromagnetic phase-transition," J. Magn. Magn. Mater. **15–18**, 415–416 (1980).

200. B. Hillebrands and K. Ounadjela, eds., *Spin Dynamics in Confined Magnetic Structures II* (Springer-Verlag, Heidelberg, 2003).